

H. Emrah Konokman · M. Murat Çoruh · Altan Kayran

Computational and experimental study of high-speed impact of metallic Taylor cylinders

Received: 9 December 2010 / Published online: 5 March 2011
© Springer-Verlag 2011

Abstract High-speed impact of metallic Taylor cylinders is investigated computationally and experimentally. On the computational side, a modular explicit finite element hydrocode based on updated Lagrangian formulation is developed. A non-classical contour integration is employed to calculate the nodal forces in the constant strain axisymmetric triangular elements. Cell and nodal averaging of volumetric strain formulations are implemented on different mesh architectures to reduce the incompressibility constraints and eliminate volumetric locking. On the experimental side, a gas gun is designed and manufactured, and Taylor impact tests of cylinders made of several metallic materials are performed. Computational predictions of the deformed profiles of Taylor cylinders and experimentally determined deformed profiles are compared for verification purposes and to infer conclusions on the effect of yield strength, strain hardening and strain rate on the material response. The article also compares the performance of different plastic flow stress models that are incorporated into the hydrocode with the experimental results and results provided by previously reported simulations and tests.

1 Introduction

Cylinder impact on an almost rigid surface is an experimental method for investigating the mechanical behavior and the dynamic yield stress of materials subjected to high strain rates typically exceeding 10^4 /s. The cylinder impact test was introduced by Taylor who studied the effect of high strain rates on the mean dynamic yield strength of metals and predicted a final profile of impacted projectiles by using only the yield strength, density of the metal and the impact velocity [1]. Conversely, Taylor's formulation could also be used to estimate the mean dynamic yield stress of the projectile material from the knowledge of the profile of the impacted cylinder, its density and the impact velocity. Taylor used momentum equilibrium equations across the plastic region to determine the mean dynamic yield stress for rigid perfectly plastic material models. Later on Hawkyard [2] employed an energy equilibrium equation across the plastic wave and came up with a solution for the strain distribution, which is considered to give somewhat better correlation with experiments.

H. E. Konokman · M. M. Çoruh
Scientific and Technological Research Council of Turkey,
Defense Industries Research and Development Institute, 06261 Ankara, Turkey
E-mail: ekonokman@sage.tubitak.gov.tr

M. M. Çoruh
E-mail: mcoruh@sage.tubitak.gov.tr

A. Kayran (✉)
Department of Aerospace Engineering, Middle East Technical University,
06531 Ankara, Turkey
E-mail: akayran@metu.edu.tr
Tel.: 90-312-2104274
Fax: 90-312-2104250

The early one-dimensional analytical treatments of Taylor impact tests provided valuable information to researchers in their effort to characterize materials at high strain rates. One-dimensional models still retain some attractive features especially in the way they offer simplicity in the interpretation of the results. The report by Jones and Gillis extends and revises prior efforts to deduce the constitutive properties of ductile metals with one-dimensional analyses [3]. In a subsequent study, Jones and Gillis [4] documented the progress that was made in developing the analytical tools to reduce data from Taylor cylinder tests. Three main categories of results presented in the report were the improvements in the experimental design of Taylor impact tests, analytical modeling to support data reduction and computational modeling to refine the constitutive behavior and to support code calculations.

The computational study of Taylor impact tests progressed in parallel with the analytical and experimental efforts to study the behavior of materials at high strain rates. Taylor impact tests were originally devised to determine the dynamic yield strength of materials at moderate strain rates. More recently, such tests have been used extensively to validate numerical codes for the simulation of plastic deformation. Computer programs *Hemp* [5], *Epic* [6], *Dyna-2D*, *LS-Dyna* [7], and *Autodyn* [8] are some examples of software that solve a wide variety of nonlinear problems in solid, fluid and gas dynamics. Fundamentals of hydrocodes are introduced in a textbook by Zukas [9]. The textbook also gives information about the existing hydrocodes that are in use. With the current status of the hydrocodes, meaningful computations can be performed. However, it is generally agreed that there is a need for improved constitutive models that describe the true behavior of different materials at high strain rates. For this purpose, many plastic constitutive models are developed and used in hydrocodes to simulate the material behavior at high strain rates. The material response for metallic materials is generally decoupled into a deviatoric part and a volumetric part. The deviatoric part of stress in the plastic regime is determined by flow stress models or the so-called strength models. The volumetric part of the stress is obtained by an equation of state that is essentially a mathematical description, with some physical basis, relating the pressure term to internal properties of the solid.

Over the years, many studies have been performed on the high strain rate response of metallic materials by using different strength models. Some examples of these studies include the work of Johnson and Holmquist who evaluated the Johnson–Cook and Zerilli–Armstrong constitutive models by comparing model predictions to tension, torsion, and cylinder impact test data [10]. Holt et al. performed an experimental and computational study of the impact deformation of titanium Taylor cylinders [11]. Celentano presented a coupled thermo-mechanical analysis of the Taylor impact tests [12].

In this article, the Taylor impact phenomenon is studied both computationally and experimentally. On the computational side a modular explicit finite element hydrocode based on an updated Lagrangian formulation is developed. A comprehensive description of the hydrocode which utilizes constant strain axisymmetric triangular elements to model the Taylor impact phenomenon is presented. A non-classical contour integration proposed in Zukas [9] is employed to calculate the nodal forces. Cell and nodal averaging of volumetric strain formulations are implemented on different mesh architectures to reduce the incompressibility constraints and eliminate volumetric locking. Currently, Johnson–Cook, Zerilli–Armstrong, Steinberg and Lund and mechanical threshold plastic flow stress models and linear, shock/polynomial Mie-Gruneisen pressure equations of state are incorporated into the hydrocode. On the experimental side, a gas gun is designed and manufactured, and Taylor impact tests of cylinders made of ETP copper, stainless steel 304L, steel 1020, aluminum 2024-T4, 6061-T6 and 7075-T3 specimens are performed at least at three different impact speeds. Experimentally and computationally determined deformed profiles are compared, and generally good agreement was observed between them. The deformed profiles are examined to infer conclusions with regard to yield strength, strain-hardening and strain rate effects on the material response. The effect of using different plastic flow stress models on the material response is studied through the comparisons made with the experimental results and through the results provided by previously reported simulations and tests.

2 Governing equations of axisymmetric dynamic problems for Lagrangian formulation

The weak form of conservation equations involves integrals over the deformed configuration. Such a formulation is commonly referred to as updated Lagrangian formulation [13].

2.1 Conservation of mass

Conservation of mass in a Lagrangian frame takes the form given by Eq. (1),

$$\rho(X, t)dV(X, t) = \rho_o(X)dV_o(X) \quad (1)$$

where dV and dV_o are the volumes of the control mass and ρ and ρ_o are densities in the current and initial states, respectively. X is the vector representing the material coordinate of the control mass.

2.2 Conservation of momentum

In axisymmetric problems, conservation of linear momentum reduces to [14]

$$\sigma_{zz,z} + \sigma_{zr,r} + \sigma_{zr}/r + \rho b_z - \rho \ddot{z} = 0, \quad (2)$$

$$\sigma_{rr,r} + \sigma_{zr,z} + (\sigma_{rr} - \sigma_{\theta\theta})/r + \rho b_r - \rho \ddot{r} = 0. \quad (3)$$

In Eqs. (2, 3) z , r and θ define the axial, radial and tangential coordinates of the axisymmetric geometry, respectively. The body forces per unit volume in the axial and radial directions are represented by b_z and b_r , respectively, and σ_{ij} are the Cauchy stress components defined for axisymmetric problems. The strong form of the momentum equation also consists of the traction boundary conditions given by Eq. (4) [13],

$$n_j \sigma_{ji} = t_i \quad \text{on } S_t \quad (4)$$

where n_j is the unit normal to the axisymmetric body and S_t is the domain over which traction boundary conditions are applied. Depending on the particular problem type, prescribed velocity or displacement boundary conditions are defined over the domain S_v subject to the condition $S_v \cap S_t = 0$. In time-dependent problems such as high-speed impact, initial conditions on the initial stress, velocity or displacements are also defined as appropriate.

2.3 Constitutive equations

Stress in the material is generally defined in terms of deviatoric and pressure part,

$$\sigma_{ii} = S_{ii} - P \quad (i = z, r, \theta; \text{no summation over } i), \quad (5)$$

where P is the pressure part of the stress tensor ($P = (\sigma_{zz} + \sigma_{rr} + \sigma_{\theta\theta})/3$) and S_{ii} are the deviatoric stresses. In high strain rate events such as impact of Taylor cylinders studied in this article, constitutive descriptions for metallic materials are made separately for the deviatoric and pressure parts. In the linear elastic regime, deviatoric stresses are expressed in rate form [15],

$$\dot{S}_{ii} = 2G \left(\dot{\epsilon}_{ii} - \frac{1}{3} \dot{V} \right) + \delta_{ii} \quad (i = z, r, \theta; \text{no summation over } i), \quad (6)$$

and shear stress is defined in rate form by

$$\dot{S}_{zr} = G \dot{\gamma}_{zr} + \delta_{zr} \quad (7)$$

where G is the shear modulus. In Eqs. (6, 7), δ terms are the stress correction terms due to the rotation of Lagrangian elements, and they are given by [15,16]

$$\delta_{zz} = -\delta_{rr} = -2S_{zr}\omega_{zr}, \quad \delta_{\theta\theta} = 0, \quad \delta_{zr} = -(S_{zz} - S_{rr})\omega_{zr} \quad (8)$$

where ω_{zr} is the rotation rate defined in the z, r plane of the axisymmetric geometry. Stress correction terms given by Eq. (8) are valid for small rotations and limited to small time steps. For explicit time integration, a first-order treatment of the incremental objectivity problem is sufficient as long as a small time step is used, which is the case in the current study.

The volumetric response for metallic materials is defined by an equation of state that relates the pressure term to internal properties of the solid. In the linear regime, the so-called linear equation of state is defined in terms of bulk modulus of elasticity as

$$P = K \cdot \mu \quad (9)$$

where K is the bulk modulus and μ is the compression defined by

$$\mu = -\frac{\Delta V}{V} = \frac{\rho}{\rho_0} - 1 = \varepsilon_{ii}. \quad (10)$$

At high pressures and dynamic events involving large deformation of metals at high strain rates and temperatures, appropriate pressure and flow stress models must be used to describe the behavior of the metals correctly. A form that has been very successful for describing metals at high pressures is the Mie-Gruneisen equation of state [15].

2.3.1 Mie-Gruneisen equation of state

The Mie-Gruneisen equation of state assumes that the material will respond as a solid throughout its loading regime. Two commonly used forms of the Mie-Gruneisen equation of state, which are also integrated in the axisymmetric Lagrangian hydrocode developed within the context of this article, are given by Eqs. (11, 12) [9, 15, 16],

$$P = (K_1\mu + K_2\mu^2 + K_3\mu^3) \left(1 - \frac{1}{2}\Gamma\mu\right) + \Gamma E_v (1 + \mu) = P_v + \Gamma E_v (1 + \mu), \quad (11)$$

$$P = \frac{\rho_0 \eta C_0^2}{(1 - s\eta)^2} \left(1 - \frac{1}{2}\Gamma\eta\right) + \Gamma E_v, \quad (12)$$

where in Eqs. (11, 12) K_i are empirical constants determined from plate impact experiments, Γ is the Gruneisen coefficient, E_v is the internal energy per initial unit volume, ρ_0 is the initial density, $\eta = 1 - \rho_0/\rho$, C_0 is the bulk sound velocity, and s is the slope of the shock velocity versus particle velocity curve. Equation (11) is generally known as the polynomial form of the Mie-Gruneisen equation of state, and Eq. (12) is known as the shock Mie-Gruneisen equation of state. It should be noted that because the pressure and internal energy are related to each other, the determination of pressure and internal energy requires simultaneous solution of the equation of state and conservation of energy equation.

2.3.2 Flow stress models

Flow stress models, which are incorporated into the hydrocode developed, are briefly introduced in this Section. For more detailed information on the flow stress models, references cited for each model should be consulted. *Johnson–Cook flow stress model* The Johnson–Cook flow stress model [17] is the most widely used and a purely empirical model expressing the yield stress in terms of plastic strain, plastic strain rate and temperature. In the Johnson–Cook model the equivalent flow stress is expressed as

$$Y = [A_{jc} + B_{jc}\bar{\varepsilon}_p^n] \cdot \left[1 + C_{jc} \ln \frac{\dot{\bar{\varepsilon}}_p}{\dot{\bar{\varepsilon}}_{p0}}\right] \cdot [1 - T^*m] \quad (13)$$

where $\bar{\varepsilon}_p$ and $\dot{\bar{\varepsilon}}_p$ are the equivalent plastic strain and strain rates, respectively, $\dot{\bar{\varepsilon}}_{p0}$ is the reference equivalent plastic strain rate which is taken as 1.0 s^{-1} [10], and T^* is the homologous temperature given by $(T - T_{ref})/(T_{melt} - T_{ref})$ for $0 \leq T^* \leq 1$, and the reference temperature is taken as the ambient temperature. Constants A_{jc} , B_{jc} , C_{jc} , n and m are the five material constants describing the behavior of metallic materials at high strain, strain rates and temperatures.

Steinberg–Guinan–Lund flow stress model The Steinberg–Guinan–Lund model [18] is a semi-empirical model, and in the rate-dependent form of this model the equivalent flow stress is given by

$$Y = [Y_T(\dot{\bar{\varepsilon}}_p, T) + Y_A f(\bar{\varepsilon}_p)] [G(P, T)/G_0] \quad (14)$$

where the athermal and thermally activated parts $Y_A f(\bar{\varepsilon}_p)$ and Y_T of the flow stress are defined by

$$Y_A f(\bar{\varepsilon}_p) = Y_A [1 + \beta(\bar{\varepsilon}_p + \bar{\varepsilon}_{ip})]^n, \quad (15)$$

$$\dot{\bar{\varepsilon}}_p = \left\{ \frac{1}{C_1} \exp \left[\frac{2U_K}{kT} \left(1 - \frac{Y_T}{Y_P} \right)^2 + \frac{C_2}{Y_T} \right] \right\}^{-1}. \quad (16)$$

Definitions and explicit expressions of the constants in Eqs. (14–16) are given in Ref. 18. The shear moduli G is defined by

$$G(P, T) = G_0 \left[1 + \frac{(G'_P/G_0) \cdot P}{\sqrt[3]{\rho/\rho_0}} - (G'_T/G_0)(T - T_{ref}) \right] \quad (17)$$

where G_0 is the shear modulus at the reference state ($T_{ref} = 300$ K, $P = 0$, $\bar{\varepsilon}_p = 0$). Primed shear moduli with the subscripts P and T imply derivatives of the shear modulus with respect to pressure or temperature at the reference state.

In this model, the equivalent flow stress is calculated iteratively. First, after determining the pressure from an equation of state, the shear modulus is calculated from Eq. (17). The thermally activated part of yield strength Y_T is then calculated from Eq. (16) iteratively. Having determined the shear modulus and Y_T , finally the equivalent flow stress is determined from Eq. (14).

Zerilli–Armstrong flow stress model The Zerilli–Armstrong flow stress model [19] is a physically based model that uses dislocation dynamics concepts and accounts for strain, strain rate and temperature effects in a coupled manner. The Zerilli–Armstrong model takes into account the differing behavior of face-centered cubic materials like copper and body-centered cubic materials like iron. For the face-centered cubic materials, the flow stress is given by Eq. (18),

$$Y = C_0 + C_2 \bar{\varepsilon}_p^n \cdot \exp(-C_3 T + C_4 T \ln \dot{\bar{\varepsilon}}_p), \quad (18)$$

and for the body-centered cubic materials the flow stress is given by Eq. (19),

$$Y = C_0 + C_1 \cdot \exp(-C_3 T + C_4 T \ln \dot{\bar{\varepsilon}}_p) + C_5 \bar{\varepsilon}_p^n. \quad (19)$$

In these relations, C_i ($i = 1 - 5$) and n are material constants with C_0 given by

$$C_0 = \sigma_g + k_h l^{-1/2} \quad (20)$$

where σ_g is the additional component of stress for the influence of solutes and initial dislocation density on the yield stress. An incremental stress contribution on the yield stress is given by the product of the micro-structural stress intensity k_h and the inverse square root of the average grain diameter l .

Mechanical threshold stress flow stress model The Mechanical threshold stress flow stress model [20] is another physically based model that considers plastic deformation to occur by the accumulation and motion of dislocations, and the rate controlling deformation mechanism to be the interactions of dislocations with defects such as grain boundaries, forest dislocations, solute atoms etc. In this model, flow stress is specified as a function of the mechanical threshold stress in the following form [21]:

$$Y = \hat{\sigma}_a + \frac{G(T)}{G_o} (S_i \hat{\sigma}_i + S_e \hat{\sigma}_e) \quad (21)$$

where G_o is the shear modulus at 0 K, $\hat{\sigma}_a$ characterizes the rate-independent component of the mechanical threshold stress, and it represents interactions of dislocations with long-range barriers such as grain boundaries. $\hat{\sigma}_i$ is the intrinsic the component of the flow stress due to barriers to thermally activated dislocation motion and dislocation–dislocation interactions, and $\hat{\sigma}_e$ represents the component of the flow stress due to micro-structural evolution with increasing deformation, that is strain hardening. In the thermally activated regime, the interaction kinetics for short-range obstacles are described by an Arrhenius expression, and the temperature and strain rate-dependent scaling factors S_i and S_e take the following form [20]:

$$S_j = \left[1 - \left(\frac{kT \ln(\dot{\bar{\varepsilon}}_{oj}/\dot{\bar{\varepsilon}}_p)}{Gb^3 g_{oj}} \right)^{\frac{1}{q_j}} \right]^{\frac{1}{p_j}} \quad j = i, e \quad (22)$$

where b is the magnitude of the Burgers vector, p_j and q_j are constants that characterize the statistically averaged shape of the obstacle profile, $\dot{\bar{\varepsilon}}_{oj}$ are constant reference strain rates, and g_{oj} are normalized activation energies that are expected to remain constant provided that the obstacle character does not vary. The thermally activated strain-hardening component of the mechanical threshold stress $\hat{\sigma}_e$ is given by

$$\frac{\partial \hat{\sigma}_e}{\partial \varepsilon_p} = \Theta_o (1 - F(\hat{\sigma}_e)) + \Theta_{IV} F(\hat{\sigma}_e) \quad (23)$$

where Θ_o is the hardening due to dislocation accumulation given by Eq. (24), and Θ_{IV} is the contribution due to stage-IV hardening,

$$\Theta_o = a_o + a_1 \log(\dot{\bar{\varepsilon}}_p) + a_2 \sqrt{\dot{\bar{\varepsilon}}_p} - a_3 T. \quad (24)$$

In Eq. (24), a_i are materials constants. To describe the structure evolution correctly, several functions F were investigated. The hyperbolic tangent function was finally chosen for the function F by Follansbee and Kocks [20] by minimizing the error between the experimental data points and the predicted $\hat{\sigma}_e - \varepsilon_p$ curve,

$$F = \tanh\left(\alpha \frac{\hat{\sigma}_e}{\hat{\sigma}_{es}}\right) / \tanh(\alpha), \quad (25)$$

where α is a material constant obtained during the curve fitting, $\hat{\sigma}_{es}$ is the saturation stress or stress at zero strain-hardening rate, and it is given by

$$\hat{\sigma}_{es} = \hat{\sigma}_{0es} \left(\frac{\dot{\bar{\varepsilon}}_p}{\dot{\bar{\varepsilon}}_{p0es}} \right)^{kT/Gb^3 g_{0es}}. \quad (26)$$

In Eq. (26), $\hat{\sigma}_{0es}$ is the saturation threshold stress for deformation at 0 K, $\dot{\bar{\varepsilon}}_{p0es}$ is the reference strain rate that is taken as the maximum strain rate, and it is usually limited to about $10^7/s$, and g_{0es} is another material constant. The model for the shear modulus $G(T)$ in Eq. (21) was developed by Varshni [22], and it has been used in conjunction with the mechanical threshold stress (MTS) flow stress model. The MTS shear modulus has the form

$$G = G_o - \frac{D}{\exp(T_0/T) - 1} \quad (27)$$

where G_o is the shear modulus at 0 K, and D and T_0 are material constants.

It should be noted that to calculate the flow stress by Eq. (21), first $\hat{\sigma}_e$ is determined by integrating Eq. (23), utilizing Eqs. (24–26).

Conservation of energy

For axisymmetric problems, the conservation of energy equation takes the form given by Eq. (28) [15],

$$\dot{E} = -P \cdot \dot{V} + V (S_{zz}\dot{\varepsilon}_{zz} + S_{rr}\dot{\varepsilon}_{rr} + S_{\theta\theta}\dot{\varepsilon}_{\theta\theta} + S_{zr}\dot{\gamma}_{zr}). \quad (28)$$

In Eq. (28), \dot{E} is the rate of internal energy and V is the current volume of the control mass and S_{ij} are the deviatoric stresses.

Weak form of the momentum equation for updated Lagrangian formulation in axisymmetric problems

The weak form of the momentum equation for an updated Lagrangian formulation is developed in the manner described by Belytschko [13]. For axisymmetric problems, the weak forms of the momentum equations can be obtained by multiplying the momentum equations (2, 3) by test functions $\delta v_i (i = z, r)$ that are the virtual velocities, integrating over the current domain, and applying the Gauss theorem. It can be shown that weak forms of the momentum equations in the axial and radial directions are given by Eqs. (29) and (30), respectively,

$$\int_{\Omega} (\delta v_{z,z} \sigma_{zz} + \delta v_{z,r} \sigma_{zr}) r dz dr - \int_{\Gamma} \delta v_z (n_z \sigma_{zz} + n_r \sigma_{zr}) d\Gamma - \int_{\Omega} \delta v_z \rho b_z dz dr + \int_{\Omega} \delta v_z \rho \dot{v}_z r dz dr = 0, \quad (29)$$

$$\begin{aligned} & \int_{\Omega} \left(\delta v_{r,r} \sigma_{rr} + \delta v_{r,z} \sigma_{zr} + \delta v_r \frac{\sigma_{\theta\theta}}{r} \right) r dz dr - \int_{\Gamma} \delta v_r (n_z \sigma_{zr} + n_r \sigma_{rr}) d\Gamma \\ & - \int_{\Omega} \delta v_r \rho b_r r dz dr + \int_{\Omega} \delta v_r \rho \dot{v}_r r dz dr = 0 \end{aligned} \quad (30)$$

where Γ is the boundary of the domain, n_z is the axial component (z) of the unit normal to the body, and n_r is the radial component (r) of the unit normal to the body.

Each integral expression in Eqs. (29) and (30) has the unit of power, and they are ascribed physical names to aid the development of finite element equations. The first integral in Eqs. (29) and (30) is defined as virtual internal power ($\delta P^{\text{int.}}$), the combination of second and third integrals is defined as virtual external power ($\delta P^{\text{ext.}}$), and the last integral is defined as virtual inertial power ($\delta P^{\text{iner.}}$) [13]. Therefore, for every virtual velocity, Eqs. (29) and (30) can be expressed as

$$\delta P^{\text{int.}} - \delta P^{\text{ext.}} + \delta P^{\text{iner.}} = 0. \quad (31)$$

3 Explicit finite element formulation

In the finite element method, the motion x_i and the displacement field u_i of an element are approximated by using interpolation functions,

$$x_i(\mathbf{X}, t) = N_I(\mathbf{X})x_{iI}(t); \quad u_i(\mathbf{X}, t) = x_i(\mathbf{X}, t) - X_i = N_I(\mathbf{X})u_{iI}(t), \quad (32)$$

where $u_{iI}(t)$ is the displacement of node I in the space dimension i ($i = z, r$). The velocities and accelerations of the nodes are obtained by the first- and second-order material time derivatives of the nodal displacements

$$\dot{u}_i(\mathbf{X}, t) = v_i(\mathbf{X}, t) = N_I(\mathbf{X})v_{iI}(t); \quad \ddot{u}_i(\mathbf{X}, t) = \dot{v}_i(\mathbf{X}, t) = N_I(\mathbf{X})\dot{v}_{iI}(t). \quad (33)$$

The discrete finite element equations are obtained by substituting the test function, which is the virtual velocity, into the weak form of momentum equations (29) and (30). Virtual velocity is not a function of time, so it can be approximated by the interpolation function yielding

$$\delta v_i(\mathbf{X}) = N_I(\mathbf{X})\delta v_{iI}. \quad (34)$$

Using the arbitrariness of the virtual nodal velocities everywhere except on the boundary where the velocities are prescribed, the virtual power equation (31) can be expressed in the axial and radial direction as

$$f_{iI}^{\text{int.}} - f_{iI}^{\text{ext.}} + f_{iI}^{\text{iner.}} = 0 \quad (i = z, r) \quad (35)$$

where the internal nodal forces in the axial and radial directions are expressed by Eqs. (36) and (37), respectively,

$$f_{zI}^{\text{int.}} = \int_{\Omega} (N_{I,z}\sigma_{zz} + N_{I,r}\sigma_{zr}) r \, dz \, dr, \quad (36)$$

$$f_{rI}^{\text{int.}} = \int_{\Omega} (N_{I,r}\sigma_{rr} + N_{I,z}\sigma_{zr} + (N_I/r)\sigma_{\theta\theta}) r \, dz \, dr. \quad (37)$$

The external nodal forces are defined by Eqs. (38) and (39), and the inertial nodal force is given by Eq. (40):

$$f_{zI}^{\text{ext.}} = \int_{\Gamma_{t_i}} N_I (n_z\sigma_{zz} + n_r\sigma_{zr}) d\Gamma + \int_{\Omega} N_I \rho b_z r \, dz \, dr, \quad (38)$$

$$f_{rI}^{\text{ext.}} = \int_{\Gamma_{t_i}} N_I (n_z\sigma_{zr} + n_r\sigma_{rr}) d\Gamma + \int_{\Omega} N_I \rho b_r r \, dz \, dr, \quad (39)$$

$$f_{iI}^{\text{iner.}} = \int_{\Omega} \rho N_I N_J \dot{v}_{iJ} r \, dz \, dr \quad (i = z, r) \quad (40)$$

where Γ_{t_i} represents the boundary where traction boundary conditions are applied. With the definitions of the internal, external and inertial nodal forces, Eq. (35) yields the following discrete equations:

$$M_{ijIJ} \dot{v}_{jJ} = f_{iI}^{\text{ext.}} - f_{iI}^{\text{int.}} \quad (i, j = z, r) \quad (41)$$

where inertial nodal forces are defined as a product of a mass matrix and the nodal accelerations,

$$M_{ijIJ} = \delta_{ij} \int_{\Omega} N_I N_J \rho \, d\Omega \quad (i, j = z, r). \quad (42)$$

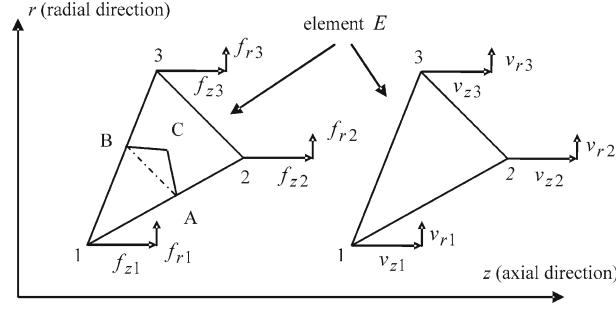


Fig. 1 Triangular element showing the nodal force, velocity components and contour definition

3.1 Discretization using axisymmetric linear triangular elements

In the present study, the Taylor impact problem is analyzed using axisymmetric constant strain linear triangular elements. The triangular coordinates are the shape functions for the linear displacement triangle, so $N_I = \xi_I$. The relation between spatial coordinates in terms of triangular coordinates and the derivatives of the shape functions are well-established relations, and they are not repeated here. Belytschko [13] has an excellent treatment of triangular three-node elements. Figure 1 presents a sample axisymmetric triangular element “E” showing the nodal force and velocity components. In the $r - z$ plane, the triangular element “E” has node numbers (1,2,3) assigned in ascending order in the counterclockwise direction. In Fig. 1 A and B are the midpoints of the element edges, and C is the geometric center of the triangular element.

For the axisymmetric triangular element, internal nodal forces given by Eqs. (36) and (37) can be cast into an internal force vector given by Eq. (43) where \bar{r} is the average radial coordinate of the three nodes of the triangular element, and $r_{IJ} = r_I - r_J$, $z_{IJ} = z_I - z_J$ and A is the current area of the triangular element. Calculation of internal nodal forces by Eq. (43) corresponds to calculating forces, which are statically equivalent to constant stresses in the triangular element, by means of contour integration. For instance, in Fig. 1 nodal forces at node “1” of element “E” are determined by means of contour integration along AB ,

$$\begin{Bmatrix} f_{z1} \\ f_{r1} \\ f_{z2} \\ f_{r2} \\ f_{z3} \\ f_{r3} \end{Bmatrix}_E^{\text{int.}} = \pi \bar{r} \begin{bmatrix} r_{23} & 0 & z_{32} & 0 \\ 0 & z_{32} & r_{23} & \frac{2}{3} \frac{A}{\bar{r}} \\ r_{31} & 0 & z_{13} & 0 \\ 0 & z_{13} & r_{31} & \frac{2}{3} \frac{A}{\bar{r}} \\ r_{12} & 0 & z_{21} & 0 \\ 0 & z_{21} & r_{12} & \frac{2}{3} \frac{A}{\bar{r}} \end{bmatrix}_E \begin{Bmatrix} \sigma_{zz} \\ \sigma_{rr} \\ \sigma_{zr} \\ \sigma_{\theta\theta} \end{Bmatrix}_E. \quad (43)$$

In the present study, the internal nodal forces are determined by adopting a slightly different contour integration that helps to increase the accuracy near the centerline [9]. The non-classical control contour cuts through the geometric center of each element and passes through the midpoints of the element edges. For instance, to calculate the internal nodal forces f_{z1} and f_{r1} at node 1 of the triangular element 123 in Fig. 1, the control contour consists of segments AC and CB , where C is the geometric center of the triangular element. The nodal forces f_{z1} and f_{r1} are then calculated as the equivalent concentrated forces that are statically equivalent to constant stresses in the triangular element by means of contour integration along segments AC and CB . For the case of axisymmetry the form of concentrated nodal forces that arise is similar but not identical to the forms that are proposed by other codes such as Epic [6]. With the new contour definition, it can be shown that the internal nodal forces on node 1 in the axial and radial directions are given by Eqs. (44) and (45),

$$f_{z1}^{\text{int.}})_E = \pi \left\{ \sigma_{zz} [(\bar{r}_{1,2} - \bar{r})(\bar{r}_{1,2} + \bar{r}) + (\bar{r} - \bar{r}_{1,3})(\bar{r} + \bar{r}_{1,3})] \right. \\ \left. + \sigma_{zr} [(\bar{z} - \bar{z}_{1,2})(\bar{r} + \bar{r}_{1,2}) + (\bar{z}_{1,3} - \bar{z})(\bar{r} + \bar{r}_{1,3})] \right\}_E, \quad (44)$$

$$f_{r1}^{\text{int.}})_E = \pi \left\{ \sigma_{rr} [(\bar{z} - \bar{z}_{1,2})(\bar{r} + \bar{r}_{1,2}) + (\bar{z}_{1,3} - \bar{z})(\bar{r} + \bar{r}_{1,3})] \right. \\ \left. + \sigma_{zr} [(\bar{r}_{1,2} - \bar{r})(\bar{r} + \bar{r}_{1,2}) + (\bar{r} - \bar{r}_{1,3})(\bar{r} + \bar{r}_{1,3})] + \frac{2}{3} A \sigma_{\theta\theta} \right\}_E \quad (45)$$

where $\bar{r} = (r_1 + r_2 + r_3)/3$, $\bar{z} = (z_1 + z_2 + z_3)/3$, $\bar{z}_{I,J} = (z_I + z_J)/2$, $\bar{r}_{I,J} = (r_I + r_J)/2$.

It should be noted that in general a node may be a vertex of a large number of elements, and in such cases nodal force contributions from all elements would be added up.

The consistent mass matrix given by Eq. (42) is expanded to full size, and it is diagonalized by the row-sum technique that conserves the total momentum, i.e. the momentum of the system with the diagonal mass is equivalent to that of the consistent mass. The nodal lumped mass at node “ I ” of the triangular element can be calculated at the initial configuration due to the Lagrangian definition of the element,

$$m_I)_E = (1/3)\rho_0 V_0 = (1/3)\rho_0 2\pi \bar{r} A_0, \quad (46)$$

where V_0 and A_0 are the initial volume and area of the axisymmetric triangular element. Equation (46) implies that one-third of the mass of the element is assigned as the nodal mass. However, Eq. (46) does not take into account the effect of the radial position of the node on the nodal mass in axisymmetric triangular elements. In axisymmetric elements, nodal mass is proportional to the radial distance from the axis of symmetry, and also for the nodes on the axis of symmetry the nodal mass should not vanish. For this reason, in the present study nodal masses are calculated by Eq. (47) which is proposed in Johnson et al. [16]. It should be noted that nodal mass calculation by Eq. (47) takes the radial position of the nodes into account,

$$m_I)_E = \left(\frac{1}{4} + \frac{1}{12} \frac{r_I}{\bar{r}} \right) \rho_0 2\pi \bar{r} A_0, \quad (47)$$

Similar to the generation of nodal internal forces, in general a node may be a vertex of many elements. In such cases, nodal mass contributions from all elements would be added up.

Finally, the external nodal forces are calculated by Eqs. (38) and (39) by applying the appropriate traction boundary conditions for the particular problem studied.

3.2 Explicit time integration of discretized momentum equations for Lagrangian mesh

Discretized momentum equations are solved by the explicit time integration using the central difference method. The detailed description of the explicit time integration is given in several references such as Zukas [9] and Belytschko et al. [13]. In this study only the key points in explicit time integration are highlighted for completeness. In the explicit time integration of discretized momentum equations, because the mass matrix is diagonal, nodal accelerations at node “ I ” are computed at the previous time step t by Eq. (48),

$$\ddot{v}_{iI}^t = \ddot{u}_{iI}^t = \frac{\sum_{n=1}^{NE} f_{iI}^{\text{ext.}})_n - f_{iI}^{\text{int.}})_n}{\sum_{n=1}^{NE} m_I)_n} \quad (i = z, r), \quad (48)$$

where “ n ” represents the counter that counts the elements sharing the common node “ I ”, and NE represents the total number of elements that share the common node “ I ”.

Nodal velocities are calculated at the half-time steps by time integration of nodal accelerations

$$v_{iI}^{t+\Delta t/2} = v_{iI}^{t-\Delta t/2} + \dot{v}_{iI}^t \Delta t \quad (i = z, r) \quad (49)$$

where it is assumed that Δt is a variable time step to assure stability of the solution as the mesh deforms.

Finally, the nodal displacements are updated by the time integration of the time-centered nodal velocities through the whole-time step,

$$u_{iI}^{t+\Delta t} = u_{iI}^t + v_{iI}^{t+\Delta t/2} \Delta t \quad (i = z, r). \quad (50)$$

3.3 Determination of updated strain rates, strains and stresses

After the determination of nodal accelerations, velocities and displacements, strain rates are calculated at the element centers of the triangular elements at half-time steps like the nodal velocities. The strain rates at the centers of axisymmetric triangular elements are determined by using the standard expressions for the gradient

in cylindrical coordinates and derivatives of the shape functions ($\xi_{I,i}; i = r, z$) for the linear displacement triangle. The resulting expression for the strain rate vector, for the element “E” in Fig. 1, is given by Eq. (51):

$$\begin{Bmatrix} \dot{\epsilon}_{zz} \\ \dot{\epsilon}_{rr} \\ \dot{\gamma}_{zr} \\ \dot{\epsilon}_{\theta\theta} \end{Bmatrix}_E = \frac{1}{2A} \begin{bmatrix} r_2 - r_3 & 0 & r_3 - r_1 & 0 & r_1 - r_2 & 0 \\ 0 & z_3 - z_2 & 0 & z_1 - z_3 & 0 & z_2 - z_1 \\ z_3 - z_2 & r_2 - r_3 & z_1 - z_3 & r_3 - r_1 & z_2 - z_1 & r_1 - r_2 \\ 0 & 2A/3\bar{r} & 0 & 2A/3\bar{r} & 0 & 2A/3\bar{r} \end{bmatrix}_E \begin{Bmatrix} v_{z1} \\ v_{r1} \\ v_{z2} \\ v_{r2} \\ v_{z3} \\ v_{r3} \end{Bmatrix}_E \quad (51)$$

where A is the current area of the triangular element “E”.

The deviatoric components of the total strain rates given by Eq. (51) are calculated at the half-time steps ($t - \Delta t/2, t + \Delta t/2, \dots$) by

$$\dot{\epsilon}_{ii} = \dot{\epsilon}_{ii} - \dot{\epsilon}_v/3 \quad (i = z, r, \theta) \quad (52)$$

where the volumetric strain rate $\dot{\epsilon}_v$ is given by $\dot{V}/V_0 = \dot{\epsilon}_{zz} + \dot{\epsilon}_{rr} + \dot{\epsilon}_{\theta\theta}$, V_0 being the initial volume of the element.

Assuming that the deformation is in the elastic range, the trial deviatoric stress components are determined at full-time steps ($t, t + \Delta t, \dots$) by integrating the generalized Hooke’s law. This process yields the updated deviatoric stress components given by Eqs. (53) and (54),

$$S_{ii}^{t+\Delta t} = S_{ii}^t + 2G\dot{\epsilon}_{ii}\Delta t + \delta_{ii}\Delta t \quad (i = z, r, \theta), \quad (53)$$

$$S_{zr}^{t+\Delta t} = S_{zr}^t + G\dot{\gamma}_{zr}\Delta t - (S_{zz}^t - S_{rr}^t)\omega_{zr}\Delta t. \quad (54)$$

In Eqs. (53) and (54) δ_{ii} are the stress correction terms due to the rotation of Lagrangian elements, and they were previously defined by Eq. (8). The rate of rotation ω_{zr} is determined at the half-time steps. For constant strain triangular elements, by using the approximations of velocities in terms of shape functions given by Eq. (33) and the derivatives of the shape functions, it can be shown that the rate of rotation for the element “E” in Fig. 1 is given by Eq. (55),

$$\omega_{zr})_E = (1/2) \left(\frac{\partial v_r}{\partial z} - \frac{\partial v_z}{\partial r} \right) = (1/4A) \left\{ v_{z1}(z_2 - z_3) + v_{r1}(r_2 - r_3) + v_{z2}(z_3 - z_1) + v_{r2}(r_3 - r_1) + v_{z3}(z_1 - z_2) + v_{r3}(r_1 - r_2) \right\}. \quad (55)$$

In the incremental elastic–plastic formulation to find out whether the trial stresses are elastic or not, the equivalent stress is calculated and compared with the yield stress $\bar{\sigma}_{\max}$, which is determined from any one of the flow stress models described earlier. The equivalent von-Mises stress is given by Eq. (56),

$$\bar{\sigma} = \sqrt{\frac{3}{2} (S_{zz}^2 + S_{rr}^2 + S_{\theta\theta}^2) + 2S_{zr}^2}. \quad (56)$$

If the calculated trial equivalent stress is lower than the yield stress determined by the flow stress model used, then the assumption that the trial stresses are elastic is correct. On the other hand, if the calculated trial equivalent stress $\bar{\sigma}$ is larger than the yield stress $\bar{\sigma}_{\max}$, the radial return method is employed and stresses are corrected as shown in Eq. (57),

$$(S_{ii})_{\text{corrected}} = (S_{ii})_{\text{trial}} \times (\bar{\sigma}_{\max}/\bar{\sigma}). \quad (57)$$

At this point, the flow stress for the next time increment ($t + \Delta t$) has to be calculated. To determine the flow stress from any one of the flow stress models equivalent plastic strain rate, equivalent plastic strain and temperature of the element have to be calculated. Plastic strain rates at half-time steps are determined by subtracting the elastic part of total strain, which is calculated from Eqs. (53) and (54) with the corrected stresses, from the total strain calculated from Eqs. (51) and (52),

$$(\dot{\epsilon}_{ii})_p = \dot{\epsilon}_{ii} - (S_{ii}^{t+\Delta t} - S_{ii}^t - \delta_{ii}\Delta t) / 2G\Delta t \quad (i = z, r, \theta), \quad (58)$$

$$(\dot{\gamma}_{zr})_p = \dot{\gamma}_{zr} - (S_{zr}^{t+\Delta t} - S_{zr}^t + (S_{zz}^t - S_{rr}^t)\omega_{zr}\Delta t) / G\Delta t. \quad (59)$$

The equivalent plastic strain rate is then calculated at half-time steps from Eq. (60),

$$\dot{\bar{\varepsilon}}_p^{t+\Delta t/2} = \sqrt{\frac{2}{9} \left[((\dot{\varepsilon}_{zz})_p - (\dot{\varepsilon}_{rr})_p)^2 + ((\dot{\varepsilon}_{zz})_p - (\dot{\varepsilon}_{\theta\theta})_p)^2 + ((\dot{\varepsilon}_{rr})_p - (\dot{\varepsilon}_{\theta\theta})_p)^2 + \frac{3}{2} \dot{\gamma}_{zr}^2 \right]}. \quad (60)$$

The equivalent plastic strain of the triangular element is calculated at full-time steps by integrating the plastic strain rate through the time step

$$\bar{\varepsilon}_p^{t+\Delta t} = \bar{\varepsilon}_p^{t+\Delta t} + \dot{\bar{\varepsilon}}_p^{t+\Delta t} \Delta t. \quad (61)$$

Assuming that the internal energy per unit original volume of the element is known, the temperature of the element at the full-time steps is calculated from Eq. (62),

$$T^{t+\Delta t} = T_0 + E_v^{t+\Delta t} / \rho_0 C_p, \quad (62)$$

where $T^{t+\Delta t}$ is the current temperature of the element at full-time steps, T_0 is the temperature when the internal energy is zero, E_v is the internal energy of the element per unit original volume at full-time steps, C_p is the specific heat of the material, and ρ_0 is the initial density of the material. At this point, it should be noted that the hydrocode also includes a heat conduction algorithm suitable for axisymmetric triangular elements. However, during the Taylor impact simulations it is experienced that because of the very fast process of the Taylor impact phenomenon, including or neglecting heat conduction did not change the results. Therefore, for brevity the description of the heat conduction algorithm is skipped in the article.

It is seen from the Mie-Gruneisen equation of state given by Eqs. (11) and (12) that pressure can be significantly affected by the internal energy. Therefore, in the present study internal energy and pressure equations are solved simultaneously for the internal energy and pressure at full-time steps. The rate of internal energy Eq. (28) is divided by the initial volume of the element V_0 , and it is expressed in incremental form as in Eq. (63),

$$E_v^{t+\Delta t} = E_v^t - \frac{P^t + Q^t}{2} (V^{t+\Delta t} - V^t) - \frac{P^{t+\Delta t} + Q^{t+\Delta t}}{2} (V^{t+\Delta t} - V^t) + (\Delta E_{dev})_v^{t+\Delta t/2}, \quad (63)$$

where Q is the artificial viscosity term that is added and $(\Delta E_{dev})_v$ is the incremental change of the deviatoric part of the internal energy per initial unit volume that is calculated at half-time steps. $(\Delta E_{dev})_v$ at half-time steps can be obtained from Eq. (28), and it is given by Eq. (64),

$$(\Delta E_{dev})_v^{t+\Delta t/2} = \Delta t [S_{zz} \dot{\varepsilon}_{zz} + S_{rr} \dot{\varepsilon}_{rr} + S_{\theta\theta} \dot{\varepsilon}_{\theta\theta} + S_{zr} \dot{\gamma}_{zr}]^{t+\Delta t/2} V^{t+\Delta t/2}, \quad (64)$$

where the deviatoric stresses S_{ij} are calculated at half-time steps by averaging the stresses at t and $t + \Delta t$, and $V^{t+\Delta t/2}$ is the current volume of the triangular element calculated at half-time steps.

To determine the internal energy of the element per unit original volume at the new time increment ($E_v^{t+\Delta t}$), the polynomial form of the Mie-Gruneisen pressure equation of state Eq. (11) is expressed at times t and $t + \Delta t$. The pressure terms are then substituted into Eq. (63) from which $E_v^{t+\Delta t}$ can be solved as

$$E_v^{t+\Delta t} = \frac{E_v^t - 0.5 [(P^t + Q^t) + (P_v^{t+\Delta t} + Q^{t+\Delta t})] \dot{\varepsilon}_v^{t+\Delta t/2} \Delta t + (\Delta E_{dev})_v^{t+\Delta t/2}}{1 + 0.5 \Gamma (1 + \mu^{t+\Delta t}) \dot{\varepsilon}_v^{t+\Delta t/2} \Delta t} \quad (65)$$

where $P_v^{t+\Delta t}$ is the part of the pressure that strictly depends on the compression μ that is already known at the new time increment $t + \Delta t$. $\dot{\varepsilon}_v^{t+\Delta t/2}$ is the volumetric strain rate at the half-time steps, and is also known because the volume of the element at times t and $t + \Delta t$ has already been determined.

Once the internal energy of the element per unit volume is determined at the new time increment from Eq. (65), the pressure at the new time increment $P^{t+\Delta t}$ can be determined from the Mie-Gruneisen pressure equation of state Eq. (11), and the temperature of the element can be determined from Eq. (62). At this point, any one of the flow stress models described earlier can be employed to calculate the flow stress $\bar{\sigma}_{\max}$ at the new time increment $t + \Delta t$. Once the flow stress is determined the corrected deviatoric stresses can be calculated by Eq. (57) at full-time steps, and stresses at the new time increment can be determined from

$$\sigma_{ii}^{t+\Delta t} = S_{ii}^{t+\Delta t} - (P^{t+\Delta t} + Q^{t+\Delta t}) \quad (i = z, r, \theta) \quad (66)$$

where the artificial viscosity Q is combined with the normal stresses to damp out localized oscillations of the concentrated masses. In the present article, artificial viscosity is incorporated in the same manner as described in previous studies such as by Wilkins [15] and Johnson et al. [16], and it is applied only when the volumetric strain rate $\dot{\epsilon}_v$ is negative. After the calculation of the stresses at the new time increment $t + \Delta t$, the updated internal nodal forces are determined from Eqs. (44) and (45), and the whole calculation process starts all over again. It should be noted that the central difference solution algorithm used in the current study is only conditionally stable. Therefore, at each solution step the time increment is checked against a minimum value given by Eq. (67) to ensure stability of the solution,

$$\Delta t = C_f \frac{\Delta s}{\sqrt{C_Q Q / \rho} + \sqrt{C_Q Q / \rho + C_s^2}}, \quad (67)$$

where Q is the artificial viscosity, C_Q is the quadratic coefficient of the artificial viscosity, C_s is sound speed of the material, ρ is the density, and Δs is the minimum length of the element, and C_f is a number taken less than unity (commonly 0.9) in order to ensure the stability of the solution [9].

3.4 Overcoming volumetric locking of triangular elements

The well-known volumetric locking problem is encountered in low-order elements for incompressible or nearly incompressible behavior in large deformation problems such as high-speed impact. In the current study, volumetric locking of linear triangular elements is treated by means of volumetric strain-averaging techniques. Two alternative volumetric strain-averaging formulations are implemented in the hydrocode developed. In the cell-averaging formulation, which is based on a mixed formulation proposed by Beissel and Johnson [23], volumetric strain is calculated as the volume average of the volumetric strains of the base triangular element and three neighboring elements that share an edge with the base element. Thus, the fundamental mesh unit consists of four triangular elements. The other averaging formulation that is implemented is the nodal averaging of volumetric strain. In the nodal-averaging formulation, at first volume averages of the volumetric strain of the elements are determined at those nodes which form the vertices of the base triangular element. Volumetric strain of the element is then calculated by taking the average of the averaged nodal volumetric strains [24,25]. In both techniques, the average volumetric strain is used to calculate the pressure for the element, and it is observed that using information from neighboring elements tends to reduce the volumetric locking substantially.

4 Sample numerical examples

Based on the theoretical formulation that is described, a single material hydrocode is developed. The hydrocode developed utilizes axisymmetric triangular elements to mesh rectangular domains that represent the axisymmetric plane of the Taylor cylinders. A mesh generator is also developed to generate triangular meshes in slashed, cross-diagonal and unstructured configurations. A detailed flowchart of the hydrocode and the list and descriptions of the subroutines are given by Konokman [14].

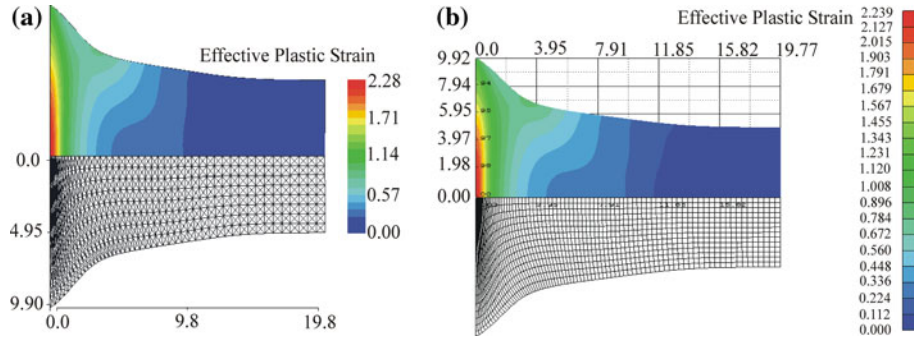
A sample Taylor cylinder impact simulation is performed by the hydrocode developed and by the commercial software Autodyn [8] to compare the results for the initial verification of the code developed. For this purpose, an axisymmetric Taylor impact simulation of OFHC copper cylinder (30 mm length, 5 mm radius) is performed. Taylor cylinders are assumed to have a striking velocity of 200 m/s, and simulations are performed at the room temperature and by assuming no friction between the cylinder and the rigid target. In the simulations, the Johnson–Cook flow stress model (Eq. (13)) and shock Mie-Gruneisen equation of state (Eq. (12)) are used. The parameters of the constitutive models used in the simulations are given in Table 1.

Figure 2 shows the effective plastic strain contours of the OFHC copper by the hydrocode developed and the Autodyn hydrocode, respectively.

Impact simulation that is performed by the hydrocode developed utilizes a cross-diagonal triangular mesh that is known to eliminate volumetric locking as long as the center node is at the intersection of the diagonals [13,27]. In the highly strained end of the Taylor cylinder the deviation of the center node away from the intersection of the diagonals increases when the mesh is coarse. However, the deviation of the center node away from the intersection of the diagonals decreases substantially when the mesh density is increased. Autodyn simulation is performed by the quadrilateral structured cells, and 1536 elements are used in both simulations.

Table 1 Constitutive model parameters of OFHC copper

Johnson–Cook flow stress model (Eq. (13)) [17]							
A_{jc} (MPa)	B_{jc} (MPa)	n	C_{jc}	m	$\dot{\epsilon}_{p0}$ (1/s)	T_0 (K)	T_{melt} (K)
90	292	0.31	0.025	1.09	1.0	298	1,356
Shock Mie–Gruneisen equation of state (Eq. (12)) [26]					Specific heat C_p (J/kg K)		
C_0 (m/s)	ρ_0 (kg/m ³)	s	Γ		383		
3,940	8,960	1.49	1.96				

**Fig. 2** Effective plastic strain contours by **a** Hydrocode developed **b** Autodyn**Table 2** Comparison of final dimensions of Taylor cylinders after impact

Hydrocode	Final length of cylinder (mm)	Radius of the impact end (mm)
Present	19.80	9.90
Autodyn	19.77	9.92

It is observed that the effective plastic strain contours determined by the two independent hydrocodes are very similar. Bulging of the OFHC copper specimens, which is an indication of the strain-hardening behavior, close to the mid-section is clearly observable in both simulations. The final length and the radius of the impact end of the Taylor cylinders are compared in Table 2. Table 2 shows that the two important dimensions of the deformed shape of the Taylor cylinders, which are determined by the present code and Autodyn, are in very close agreement.

The comparison of deformed profiles of Taylor cylinders is also presented for another OFHC copper cylinder that is 23.47 mm in length and 7.62 mm in diameter [28] and for a higher impact speed of 250 m/s. Figure 3 gives the comparison of the deformed profiles that are obtained by the hydrocode developed and Autodyn software using the constitutive model parameters given in Table 1. From Fig. 3, it can be seen that the deformed profiles obtained by the hydrocode and the Autodyn software are in perfect agreement.

In the Taylor impact simulations of the OFHC copper a room temperature constant specific heat (C_p) of 383 J/kg K is used. However, the specific heat versus temperature curve of OFHC copper has a mild positive slope above 250 K. Therefore, to see the effect of specific heat on the final temperature and final deformed shape of the cylinders, Taylor simulations are also performed by using a specific heat value of 414 J/kg K, which is considered to be an appropriate constant value used at temperatures above 250 K and below 700 K [28]. For the particular case study, an OFHC copper cylinder that has a length of 30 mm, radius of 4 mm is used, and the impact speed is taken as 200 m/s. The temperature distributions and final deformed profiles that are obtained by using two different constant specific heat values are compared in Fig. 4. The results shown in Fig. 4 are obtained with the use of cross-triangular elements in the mesh.

Figure 4 shows that with the use of slightly higher constant specific heat than the room temperature value a slight temperature drop is observed over the cylinder, as expected. However, the final deformed length, maximum final radius and deformed profiles are very close to each other. Therefore, the use of constant room temperature specific heat is considered to be appropriate for the impact speeds used in the present study.

The implementation of nodal averaging of volumetric strain, to prevent volumetric locking, is demonstrated for the same OFHC copper cylinder. The simulations are repeated with a slashed triangular mesh arrangement with and without nodal averaging of volumetric strain. Table 3 summarizes the final length and the radius of the mushroomed end of the cylinders, and Fig. 5 shows the deformed shapes and final temperature distribution in the cylinders, which are determined by the slashed triangular mesh arrangement with and without nodal

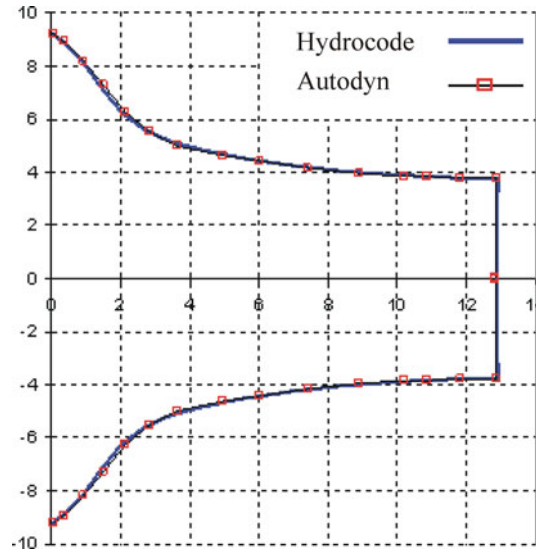


Fig. 3 Comparison of deformed profiles calculated by the hydrocode developed and Autodyn

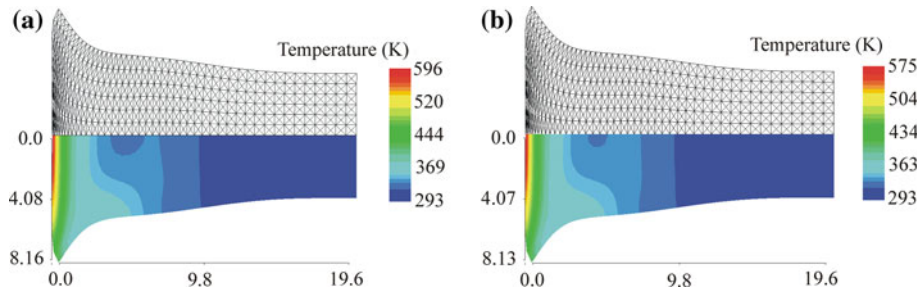


Fig. 4 Final temperature distribution in OFHC copper **a** 383 J/kg.K, **b** 414 J/kg.K (initial length/radius: 30 mm/4 mm, impact speed: 200 m/s)

Table 3 Deformed dimensions of cylinders obtained with different element arrangements

Element arrangement	Final length of cylinder (mm)	Radius of the impact end (mm)
Cross-triangle	19.6	8.16
Slashed-without averaging	20.3	7.47
Slashed-with nodal averaging	19.6	8.10

averaging of the volumetric strain. In the simulations, for the OFHC copper a room temperature specific heat value of 383 J/kg.K is used.

It can be observed from Table 3 and Figs. 4a and 5 that the solution obtained by the slashed triangular mesh without nodal averaging of volumetric strain shows clear signs of volumetric locking. The final length of the cylinder is longer, and the mushroomed end radius is shorter compared to the results obtained with the cross-triangle and slashed triangular mesh arrangement with nodal averaging of volumetric strain. It is seen that by implementing nodal averaging of volumetric strain in the slashed triangular mesh solution, critical metrics such as final length and impact end radius of the cylinder approach to the values obtained by a cross-triangular mesh arrangement that is known to eliminate volumetric locking significantly [13,27]. It is also observed that the temperature distributions obtained, by the cross-triangular elements (Fig. 4a) and slashed triangular mesh solution with nodal averaging of volumetric strain (Fig. 5a), are very close to each other. The maximum temperatures at the impact end are also very close to each other. On the other hand, the solution obtained with a slashed arrangement of triangular elements, without nodal averaging of volumetric strain (Fig. 5b), underestimates the maximum temperature at the impact end where the volumetric locking is most severe. Careful observation of Fig. 5 also reveals that as expected away from the impact end at the same axial locations temperatures determined by the slashed triangular mesh without nodal averaging of volumetric strain

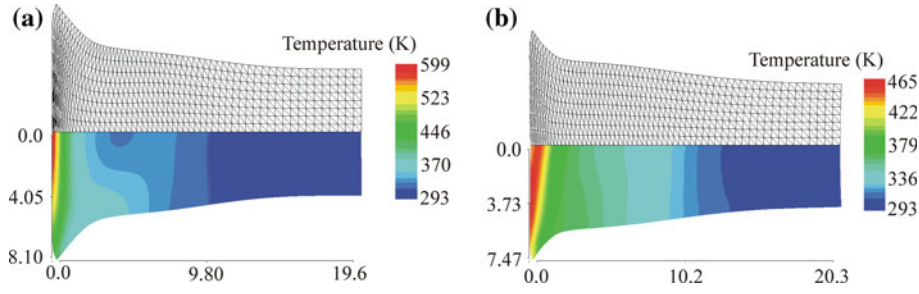


Fig. 5 Deformed profiles and final temperature distribution in OFHC copper **a** Slashed arrangement with nodal averaging **b** Slashed arrangement without nodal averaging (initial length/radius: 30 mm/4 mm, impact speed: 200 m/s)

Table 4 Constitutive model parameters of Armco iron

Johnson–Cook flow stress model (Eq. (13)) [17]				m	$\dot{\epsilon}_{p0}$ (1/s)	T_0 (K)	T_{melt} (K)
A_{jc} (MPa)	B_{jc} (MPa)	n	C_{jc}				
175	380	0.32	0.06	0.55	1.0	298	1,811
Shock Mie–Gruneisen equation of state (Eq. (12)) [29]				Specific heat C_p (J/kg K)			
C_0 (m/s)	ρ_0 (kg/m ³)	s	Γ	452			
3,570	7,850	1.92	1.8				

are higher than temperatures determined by the slashed triangular mesh with nodal averaging of volumetric strain.

Another numerical example is performed to demonstrate and compare the performances of the cell and the nodal averaging of volumetric strain formulations that are used to reduce volumetric locking. For this purpose, an Armco iron cylinder model having a length of 30 mm and radius of 5 mm is used, and the initial impact speed is taken as 250 m/s. In the simulations, the Johnson–Cook flow stress model (Eq. 13) and the shock Mie–Gruneisen equation of state (Eq. (12)) are used. The parameters of the constitutive models used in the simulations are given in Table 4.

For this particular example, an unstructured stretched triangular mesh is generated by the mesh generator developed. Unstructured triangular elements are popular because they can fit bodies with complex contours. The solution mesh is stretched along the axis of the cylinder such that the fine mesh is used near the impact end of the cylinder where large deformation and high strain rate effects are dominant, away from the impact end the mesh is made coarser. The stretched mesh is very useful in terms of decreased solution time since the solution domain has a smaller number of elements and nodes compared to the uniform mesh case. Deformed plots of Taylor cylinders are determined by employing three different volumetric strain calculations; standard calculation of volumetric strain without averaging of volumetric strain, and cell and nodal averaging of volumetric strains, respectively. Figure 6 shows the final deformed plots and the effective plastic strain distributions of the results from the three different volumetric strain formulations. It is observed that by employing cell and nodal averaging of volumetric strain formulations volumetric locking can be reduced effectively. Standard calculation of volumetric strain causes volumetric locking as evidenced by the shorter mushroomed end radius. By employing averaging schemes, the mushroomed end radius is seen to increase due to the elimination of volumetric locking that is most severe near the impact end of the cylinder where there is large deformation. It should also be noted that unstructured triangular elements cause jagged plastic strain contours. However, by employing cell and nodal averaging of volumetric strain formulations plastic strain contours, although still somewhat jagged, become smoother compared to the plastic strain contours obtained without employing volumetric strain-averaging schemes.

The implementation of nodal and cell averaging of volumetric strain techniques is demonstrated in detail by Konokman et al. [14,30] for the solution of the Taylor impact problem with axisymmetric slashed triangular and unstructured triangular meshes.

5 Taylor impact experiments

Taylor impact experiments are performed by means of a gas gun which is designed and manufactured. Figure 7 shows the schematic drawing of the Taylor impact set-up which consists of a pressure reservoir, a barrel, a

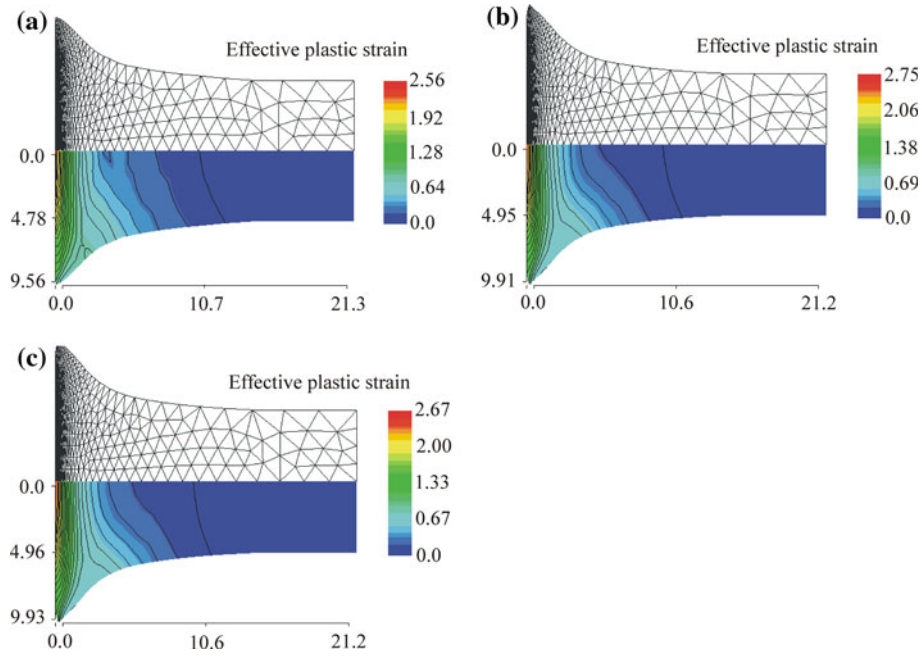


Fig. 6 Deformed profiles and effective plastic strain contours in Armco iron **a** Without averaging of volumetric strain **b** With cell averaging of volumetric strain **c** With nodal averaging of volumetric strain

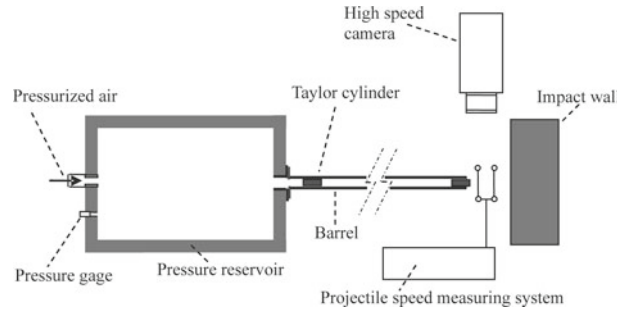


Fig. 7 Schematic drawing of the Taylor impact test set-up

Table 5 Materials used in Taylor cylinders

Material	Type
Copper	ETP
Steel	1020, 304L
Aluminum	2024-T4, 6061-T6, 7075-T6

Initial cylinder length/radius: 30 mm/4.85 mm

pressure release section, two separate projectile velocity determination systems and an impact wall. It should be noted that in order to reach impact speeds in the range of 200–300 m/s within a reasonable barrel length, sudden application of the pressurized gas on the Taylor cylinder is required. Therefore, a special pressure release section is designed at the barrel exit of the pressure reservoir to achieve sudden application of the pressure. For accurate determination of the impact speed, two separate systems are used to measure the speed of the Taylor cylinder after exiting the barrel and before hitting the impact wall. A hardened steel block is used as the impact wall. The impact face of the block is machined to have a smooth surface in order to achieve low friction condition during impact. The experimental set-up is introduced in more detail by Konokman [14].

Taylor impact tests are performed by firing cylinders made of different metallic materials given in Table 5. For each material, Taylor impact tests are performed at least at three different impact speeds. For the materials listed in Table 5, Figs. 8, 9, 10, 11, 12, 13 show the profiles of the Taylor cylinders after impact and the impact velocities measured.

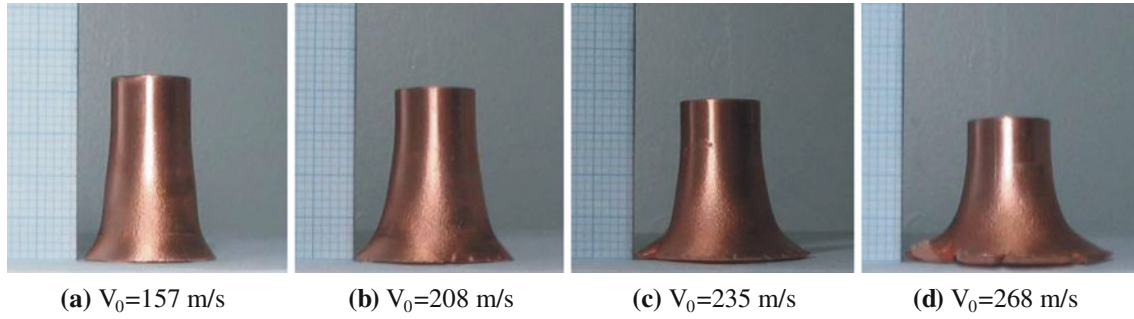


Fig. 8 Profiles of ETP copper specimens after impact

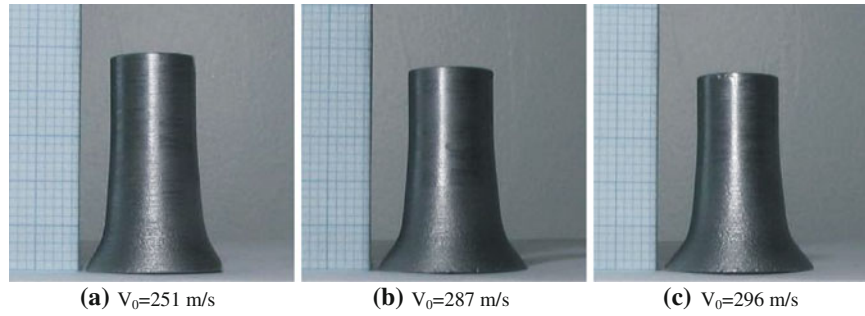


Fig. 9 Profiles of steel 1020 specimens after impact

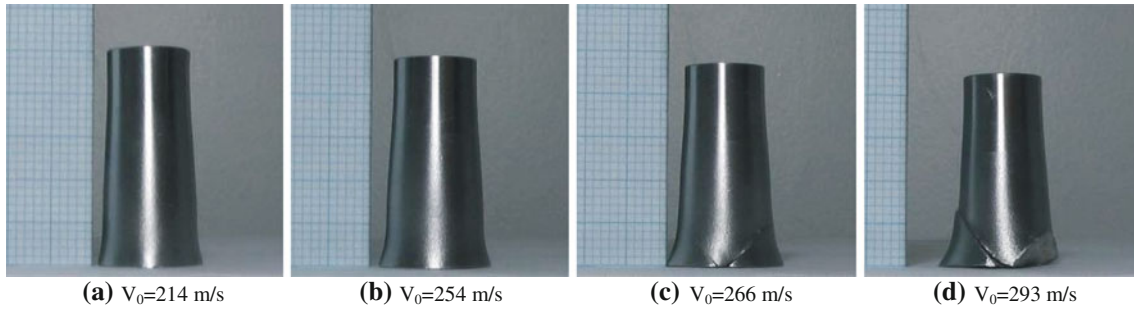


Fig. 10 Profiles of steel 304L specimens after impact

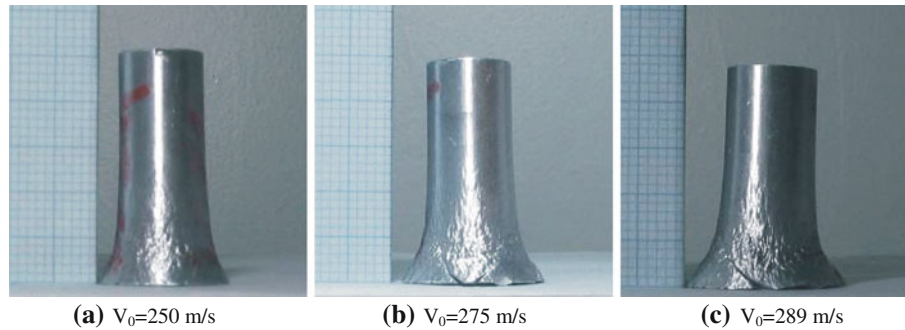


Fig. 11 Profiles of Aluminum 2024-T4 specimens after impact

Figure 14 shows the plot of the variation of ratios of the final length of the Taylor cylinders (L_{final}) to the initial length (L_0) with respect to the initial kinetic energy density of the specimens. It is observed that in the initial kinetic energy density ranges where the Taylor impact tests are conducted, almost a linear relationship exists between the length ratios and the initial kinetic energy density. Such a relationship has also been reported

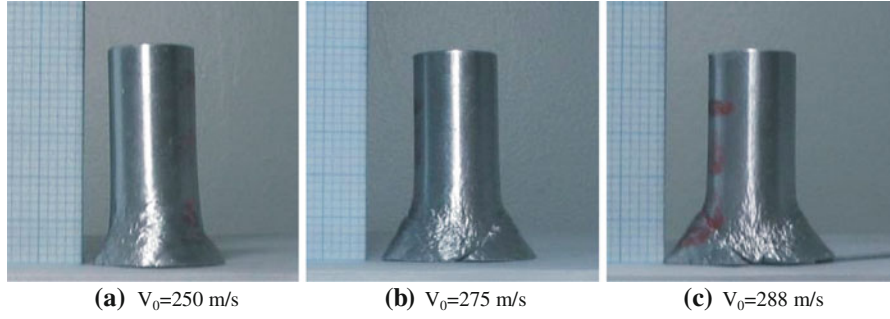


Fig. 12 Profiles of Aluminum 6061-T6 specimens after impact

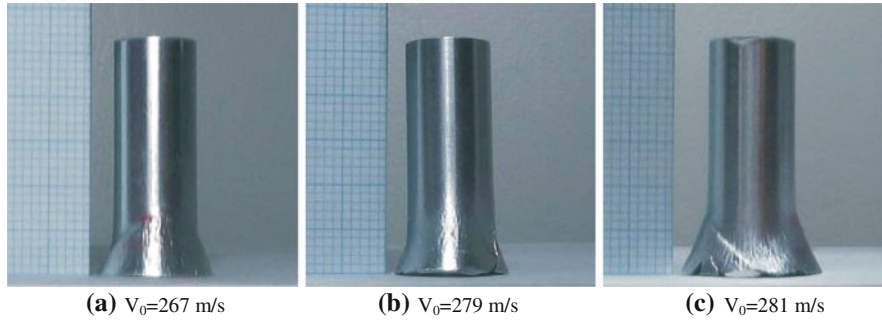


Fig. 13 Profiles of Aluminum 7075-T6 specimens after impact

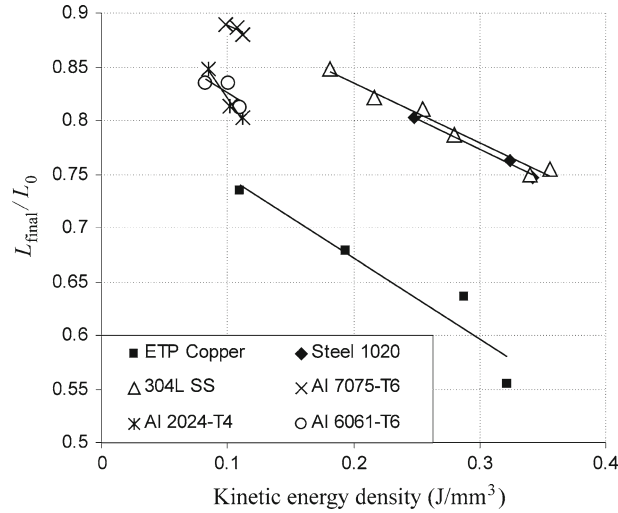


Fig. 14 Final length to initial length ratio versus initial kinetic energy density

by Banerjee [28] who gathered length ratio versus kinetic energy density data from a number of Taylor impact tests performed by other groups. At this stage, it should be noted that the momentum equilibrium theory of Taylor [1] and the energy-based theory for the mushrooming of Taylor cylinders reported by Hawkyard [2] predict a slightly nonlinear variation of the length ratio with the kinetic energy density. However, if Figs. 6 and 12 of Hawkyard [2] are studied carefully, it can be seen that for the initial kinetic energy density ranges used in the current study, the variation of the length ratio with the kinetic energy density can be approximated by an almost linear relationship that supports the current experimental finding. The ratios of the final end radius to the initial radius with respect to the initial kinetic energy density also shows almost linear variation but with positive slope.

The deformed profiles of the specimens provide valuable qualitative information about the strength and strain rate characteristics of the materials. Final lengths of the specimens give a clue with regard to the yield

strength and strain rate dependency of the flow stress. For nearly the same initial kinetic energy density, a higher final length of the specimen is an indication of higher yield strength. For instance, Fig. 14 shows that in case of aluminum alloys that have close initial kinetic energy densities, it is observed that Taylor cylinders made of Al 7075-T6 have the highest final length compared to the final lengths of specimens made of alloys 2024-T4 and 6061-T6. This experimental observation is in accordance with the fact that the aluminum 7075-T6 has a much higher yield strength compared to aluminum 2024-T4 and 6061-T6 that have close yield strengths. For materials that have high strain rate dependency, strength of the materials is more pronounced when the strain rate is higher. Slopes of the length ratio curves also give qualitative clue about the strain rate dependency of the materials. In the Taylor impact test the strain rate is proportional to the impact speed. Therefore, it can be concluded that the smaller the slope of the variation of the length ratio with the initial kinetic energy density, the higher the effect of the strain rate.

For instance, Fig. 14 shows that stainless steel 304L and steel 1020 have similar length ratio versus initial kinetic energy density slopes implying similar strain dependency, which is indeed the case because Johnson–Cook strain rate constants C of steel 304L and 1020 are known to be close to each other. However, in the current study more experimental data are needed to have an accurate assessment on the comparison of the strain rate dependency of the flow stress of the materials tested. It is known that copper shows significant strain-hardening and strain rate sensitivity of plastic flow behavior. It can be clearly seen from Fig. 8 that the peripheral bulging of the copper specimen close to the mid-section of the cylinder is a clear indication of the strain-hardening behavior. Comparison of Figs. 9 and 10 reveals that steel 1020 and stainless steel 304L show different strain-hardening behavior. Stainless steel 304L has more distinct peripheral bulging compared to steel 1020, which is a clear indication of a higher strain-hardening property of steel 304L. This observation is also verified by the knowledge that 304L stainless steel has a higher strain-hardening coefficient compared to that of 1020 steel [31]. Aluminum alloys are known to be low strain-hardening materials that are relatively strain rate insensitive [32]. Figures 11, 12, 13 show that the peripheral bulging of aluminum specimens is barely visible, which confirms the low strain-hardening behavior of aluminum alloys. Among the aluminum alloys tested, Al 2024-T4 exhibited the most observable peripheral bulging. An interesting phenomenon which occurred during the Taylor impact tests was the formation of shear cracks in some of the specimens. Figures 10, 11, 12, 13 clearly show the 45° shear cracks on the lateral surface of the cylinders that are fired with higher impact speeds. In some specimens, shear cracking resulted in fragmentation of the impact end of the projectile. The present experimental observation of shear crack formation is consistent with the numerical prediction of shear crack formation by Teng et al. who also referenced experimental results in their article on the formation of shear cracking, which is identified as one of the possible fracture modes in the Taylor test [33].

6 Taylor impact simulations and comparisons with experiments

In this Section for brevity some selected Taylor impact simulations and a comparison of some of the experimental results and the simulation results are presented. A complete set of Taylor impact simulations is given by Konokman [14].

6.1 Simulations with different mesh resolutions

A mesh resolution study is demonstrated for the OFHC copper cylinder using the constitutive model parameters given in Table 1. Simulations are performed at an impact speed of 200 m/s. Taylor impact simulations at the room temperature are performed with cross-diagonal triangular mesh with different mesh resolutions, and the change of the critical solution parameters is monitored. Table 6 gives the summary of the mesh resolution study for the uniform mesh case. The last three columns of Table 6 present the final deformed length, the final maximum radius of the Taylor cylinder at the impact end, and maximum effective plastic strain values, respectively.

Table 6 shows that by increasing the number of elements used in the simulations, the final length, the maximum radius of the cylinder and maximum effective plastic strain values increase slightly and converge smoothly. It should be noted that volumetric locking also occurs with a cross-triangular element arrangement with coarse mesh, and this is evident from the smaller maximum radius for coarser meshes compared to finer meshes. As pointed out by Beissel and Johnson [23], the ratio of the final maximum diameter to the initial diameter is a good measure of volumetric locking, whereas the ratio of the final deformed length to initial

Table 6 Mesh resolution study of Taylor impact simulations

Elements	Nodes	CPU time (s)	L_{final} (mm)	R_{max} (mm)	Max. effective plastic strain
96	63	0.36	19.76	9.65	1.94
864	475	16.44	19.78	9.87	2.27
1,536	825	55.56	19.80	9.90	2.28
2,400	1,271	150.58	19.81	9.92	2.29
4,704	2,451	723.17	19.83	9.94	2.30

Initial cylinder length/radius: 30 mm/5.0 mm

length is not such a good measure. It is known that in order for the cross-triangular elements not to lock the center node should be on the intersection of the diagonals [13]. When cross-triangular elements are used in the solution domain, some elements that are close to the impact end may deform in such a way that the center node may move away from the intersection of the diagonals. For coarse meshes, the deviation of the center node away from the intersection of the diagonals is higher. Therefore, for coarse meshes the effect of volumetric locking can be seen even though cross-triangular elements are used. When the mesh density is increased, the deviation of the center node away from the intersection of the diagonals becomes very small if a suitably fine mesh is used. Table 6 shows that as the mesh is made finer, the final maximum radius increases, and this is a sign of reduced volumetric locking.

It should also be noted that in isochoric plasticity the volume of the cylinder should be preserved. Results given in Table 6 show that as the mesh density is increased both the final deformed length and the maximum radius increase, and this observation may raise questions with regard to volume preservation. However, the comparison of the deformed profiles determined by the coarse and the fine mesh cases revealed that although the coarse mesh case has small maximum radius, the deformed profile of the coarse mesh case is slightly over the deformed profile of the fine mesh case along the middle section of the cylinder for a longer distance. For the coarse mesh case, slightly more bulging out of the deformed profile, compared to the fine mesh case, in the middle section of the cylinder compensates the lowering of the volume near the impact end.

6.2 Comparison of flow stress models

The effect of using different flow stress models on the critical metrics such as the final length and the diameter of the mushroomed end of the deformed cylinder is demonstrated by Taylor impact simulations of OFHC copper specimens. For the comparison of flow stress models, OFHC copper is selected because it is a well-characterized material showing significant strain hardening, strain rate sensitivity and temperature dependence of plastic flow behavior. Simulations are performed at the room temperature and at an impact speed of 220 m/s. Simulations are repeated with four different flow stress models that are described in Sect. 2, and the Mie-Gruneisen pressure equation of state is used for each case. For the Johnson–Cook strength model, the parameters given in Table 1 are used. Zerilli–Armstrong, Steinberg–Guinan–Lund and mechanical threshold flow stress parameters for OFHC copper that are used in the simulations are presented in Table 7.

Table 7 Flow stress model parameters of OFHC copper

Zerilli–Armstrong (Eq. (18)) [19,34]									
C_0 (MPa)	C_2 (MPa)	C_3 (1/K)	C_4 (1/K)	n					
117	890	0.0028	0.000115	0.5					
Steinberg–Guinan–Lund (Eqs. (14–17)) [18,28]									
G_0 (GPa)	Y_A (MPa)	β	$\bar{\epsilon}_{ip}$	U_K (eV)	n				
47.7	125	36	0	0.31	0.45				
C_1 (1/s)	C_2 (MPa s)	Y_p (MPa)	G'_p/G_0 (1/Pa)	G'_T/G_0 (1/K)	T_{ref} (K)				
0.71e6	0.012	20	2.8e-11	3.8e-04	300				
Mechanical threshold (Eqs. (21–27)) [20,28]									
$\hat{\sigma}_a$ (MPa)	G_0 (GPa)	$\hat{\sigma}_i$ (MPa)	b (nm)	g_{0i}	g_{0e}	p_i	q_i	p_e	q_e
40	51.3	0.0	0.256	1	1.6	1	1	2/3	1
$\dot{\epsilon}_{oi}$ (1/s)	$\dot{\epsilon}_{oe}$ (1/s)	a_0 (GPa)	a_1 (MPa log(s))	a_2 (MPa \sqrt{s})	a_3 (MPa/K)	α			
1.0	1.0e07	2.39	12	1.696	0.0	2			
Θ_{IV} (Pa)	g_{0es}	$\hat{\sigma}_{0es}$ (MPa)	$\dot{\epsilon}_{p0es}$ (1/s)	D (GPa)	T_0 (K)				
0.0	0.2625	770	1.0e07	3	165				

Table 8 Comparison of geometric metrics determined by the flow stress models

Flow stress model	Present study ^a $V_0 = 220$ m/s				Banerjee ^b [28] $V_0 = 210$ m/s			
	L_{final} (mm)	L_{final}/L_0	R_{max} (mm)	R_{max}/R_0	L_{final} (mm)	L_{final}/L_0	R_{max} (mm)	R_{max}/R_0
Johnson–Cook	18.48	0.62	10.92	2.18	15.2	0.65	7.8	2.05
Zerilli–Armstrong	19.14	0.64	9.70	1.94	14.8	0.63	7.0	1.84
Steinberg–Guinan–Lund	19.10	0.64	9.53	1.91	15.4	0.66	6.8	1.78
Mechanical threshold	18.12	0.60	9.91	1.98	14.4	0.61	7.2	1.89

^aInitial cylinder length/radius: 30 mm/5.0 mm^bInitial cylinder length/radius: 23.47 mm/3.81 mm

Table 8 summarizes the qualitative comparison of the final length and the radius of the mushroomed end of deformed cylinders that are determined by three different flow stress models and results by Banerjee [28].

Table 8 shows that the mechanical threshold flow stress model predicts the smallest final deformed length of the cylinder, whereas the Johnson–Cook model predicts the largest final mushroom diameter. Qualitatively, these conclusions are in accordance with the results obtained by other independent studies [28]. It should also be noted that the effect of using different flow stress models on the final length and radius of the mushroomed end of the deformed cylinders follows the same pattern in both the present study and in Ref. [28], except for the final length of the Taylor cylinder predicted by the Zerilli–Armstrong model. Banerjee’s report presents Taylor impact simulation results that are determined by the material point method and experimentally deformed profiles of Taylor cylinders made of OFHC copper. The final length of the Taylor cylinder determined by Banerjee using the Zerilli–Armstrong model is less than the final lengths predicted by the Johnson–Cook and Steinberg–Guinan–Lund models but higher than the final length predicted by the mechanical threshold model. However, in the present study simulation performed by using the Zerilli–Armstrong flow stress model predicts the highest final length of the deformed cylinder. This discrepancy is attributed to using different initial yield strengths in the present study and by Banerjee [28]. In the present study for the Zerilli–Armstrong flow stress model the initial temperature and strain rate independent yield strength C_0 is calculated as 117 MPa from Eq. (20) by using an average grain diameter of 5 μm , which is given by Frutschy and Clifton [34]. However, Banerjee [28] and Zerilli and Armstrong [19] used an initial yield strength of 65 MPa. Therefore, in the current study the higher final length of the deformed cylinder calculated by using the Zerilli–Armstrong flow stress model is due to the use of higher initial yield strength.

6.3 Comparison of Taylor impact simulations and experiments

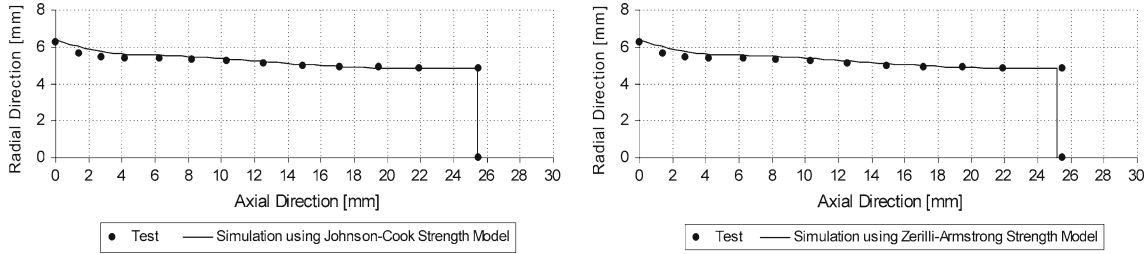
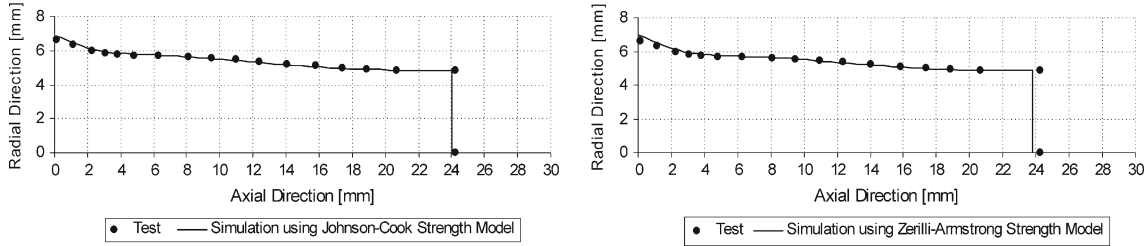
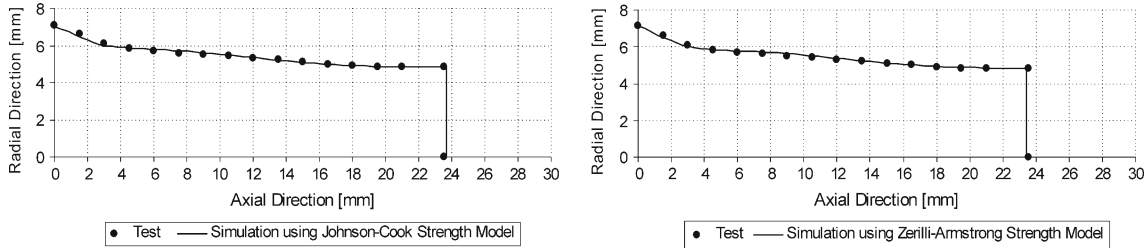
In this Section, deformed profiles of the test specimens are compared with the deformed profiles determined by Taylor impact simulations to infer conclusions about the accuracy of the hydrocode developed and to provide data on Taylor impact results of metallic materials such as steel and aluminum for which less data exist in the literature compared to copper. The most common comparison of the deformed profiles is the “view graph norm” in which a plot of the deformed profile which is determined by the simulations is superimposed on the experimentally determined deformed profile, and a visual judgment of accuracy is made. The final length of the deformed profile and radius of the mushroomed end are also used as the two most common geometrical metrics in the quantitative comparison of the deformed profiles. It should be noted that in the present study Taylor impact simulations are performed for at least three different impact speeds and using four different flow stress models. Therefore, in the article only some selected comparisons are presented for those material-constitutive model pairs for which the constitutive model parameters could be found in the literature.

The first comparison of the experimentally and computationally determined profiles of the deformed Taylor cylinders is given for stainless steel 304L. For the stainless steel 304L, Taylor impact simulations are performed by using Johnson–Cook and Zerilli–Armstrong plastic flow stress models, and the shock Mie–Gruneisen pressure equation of state. Table 9 gives the parameters of the constitutive models used in the simulations.

For three different impact speeds, Figs. 15, 16, 17 give the plots of the computationally determined deformed profiles of Taylor cylinders made of stainless steel 304L in continuous curves, superimposed on the experimentally determined deformed profiles which are shown by dots at discrete locations along the cylinder axis.

Table 9 Flow stress model parameters of stainless steel 304L

Johnson–Cook model (Eq. 13) [35]							
A_{jc} (MPa)	B_{jc} (MPa)	n	C_{jc}	m	$\dot{\epsilon}_{p0}$ (1/s)	T_0 (K)	T_{melt} (K)
310	1,000	0.65	0.07	1.	1.0	293	1,673
Zerilli–Armstrong (Eq. 18) [36]							
C_0 (MPa)	C_2 (MPa)	C_3 (1/K)	C_4 (1/K)	n	σ_g (MPa)	k_h (MPa $m^{0.5}$)	l (μm)
60	2340	0.0016	0.00008	0.36	−76.9	0.75	30
Shock Mie–Gruneisen equation of state (Eq. 12) [34]						Specific heat C_p (J/kg K)	
C_0 (m/s)	ρ_0 (kg/m 3)	s	Γ			440	
4,570	7,900	1.49	2.17				

**Fig. 15** Computationally and experimentally determined profiles of steel 304L- $V_0 = 214$ m/s**Fig. 16** Computationally and experimentally determined profiles of steel 304L- $V_0 = 254$ m/s**Fig. 17** Computationally and experimentally determined profiles of steel 304L- $V_0 = 266$ m/s

Figures 15, 16, 17 show that there is a high degree of agreement between the deformed profiles that are determined experimentally and computationally. Both Johnson–Cook and Zerilli–Armstrong flow stress models performed very well for stainless steel 304L. It is observed that the Zerilli–Armstrong flow stress model slightly underestimates the final deformed length of the Taylor cylinder made of stainless steel 304L. Both flow stress models predict the peripheral bulging of the specimens quite accurately.

The second comparison of the experimentally and computationally determined profiles of the deformed Taylor cylinders is given for aluminum 6061-T6. For aluminum 6061-T6, Taylor impact simulations are performed by using the Johnson–Cook plastic flow stress model and the shock Mie–Gruneisen pressure equation of state. The parameters of the constitutive models of Al 6061-T6 used in the simulations and their references are given in Table 10. Parameters of the Mie–Gruneisen equation of state are taken from Banerjee [38] where reference is made to the data used in Alegria [39].

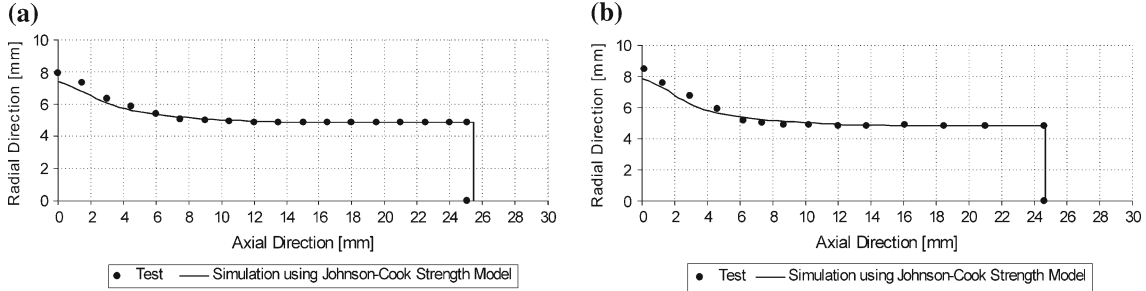
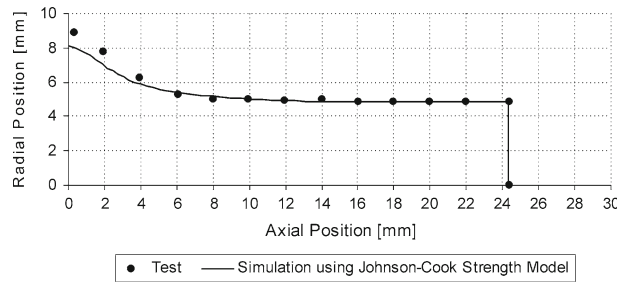
Table 10 Flow stress model parameters of aluminum 6061-T6

Johnson–Cook model (Eq. (13)) [40]

A_{jc} (MPa)	B_{jc} (MPa)	n	C_{jc}	m	$\dot{\epsilon}_{p0}$ (1/s)	T_0 (K)	T_{melt} (K)
289.6	203.4	0.35	0.011	1.34	1.0	294.2	925.4

Shock Mie-Gruneisen equation of state (Eq. (12)) [38]

C_0 (m/s)	ρ_0 (kg/m ³)	s	Γ
5,386	2,700	1.339	1.99

Specific heat C_p (J/kg K)
896**Fig. 18** Computationally and experimentally determined profiles of Al 6061-T6 **a** $V_0 = 250$ m/s **b** $V_0 = 275$ m/s**Fig. 19** Computationally and experimentally determined profiles of Al 6061-T6- $V_0 = 288$ m/s

For three different impact speeds, Figs. 18 and 19 give the plots of the computationally and experimentally determined deformed profiles of cylinders made of aluminum 6061-T6. For aluminum 6061-T6 except near the mushroomed end of the Taylor cylinders where shear cracks are observed, experimentally and computationally determined profiles agree very well even though currently no damage model exists in the hydrocode developed. The discrepancy near the impact end is mainly attributed to the fracture-petaled region that made it hard to make accurate measurements of the deformed profile. As it is seen in Fig. 12, aluminum 6061 specimens had a shear crack formation that mostly ended in fragmentation. Therefore, radial distance measurements, near the fracture petaled region, are larger than the simulation results. The low strain-hardening property of aluminum 6061-T6 is also evident from almost nonexistent peripheral bulging which is also captured in the simulation results. It should be noted that since aluminum has lower density compared to steel or copper, higher impact speeds would be required to have a similar kinetic energy density of aluminum specimens as the steel or copper specimens. Peripheral bulging of aluminum specimens could then be observed at higher kinetic energy densities. However, based on the experimental experience, at higher speeds fragmentation of the Taylor cylinders made of aluminum alloys would occur, and it would be very difficult to identify the peripheral bulging.

7 Conclusions

A computational and experimental study of the Taylor impact phenomenon has been presented. An explicit finite element hydrocode based on an updated Lagrangian formulation is developed. The hydrocode is initially validated by comparing the Taylor impact simulation results of OFHC copper obtained by the developed hydrocode with the results of the commercial software Autodyn, and excellent agreement has been found. To reduce the incompressibility constraints and prevent volumetric locking, cell and nodal averaging of volumetric

strain techniques are employed for the slashed and unstructured triangular meshes that are known to exhibit significant volumetric locking.

Taylor impact tests of ETP copper, stainless steel 304L, steel 1020, aluminum 2024-T4, 6061-T6 and 7075-T3 specimens have been performed at room temperature by means of a gas gun that is designed and manufactured as part of the current study. Deformed profiles of the test specimens are compared with the deformed profiles determined by Taylor impact simulations, and it is observed that experimentally and computationally determined profiles agree reasonably well. In some test specimens, due to the shear crack formation and fragmentation, an accurate measurement of the deformed profile near the impact end could not be made. Therefore, the discrepancy in the deformed profiles of some specimens near the impact end and especially in the final mushroomed radius is partly attributed to the difficulty in accurate measurement of the deformed profile of the specimens with shear crack formation.

Based on the experimental and computational findings, the strain-hardening effect on the material response of Taylor cylinders is evident from the peripheral bulging near the mid-section of the cylinders. For instance, stainless steel 304L showed very distinct peripheral bulging compared to steel 1020, which is a clear indication of a higher strain-hardening property of steel 304L. Aluminum alloys showed barely visible peripheral bulging, which indicates low strain-hardening behavior. Experimental results also showed that almost a linear variation, with negative slope, exists between the length ratio and the kinetic energy density in the kinetic energy density range studied. It is concluded that flattening of the length ratio versus kinetic energy density curve is a sign of a higher effect of strain rate dependency on the material response. Stainless steel 304L and steel 1020 had similar length ratio versus initial kinetic energy density slopes implying similar strain dependency, which is indeed the case because the Johnson–Cook strain rate constants C of steel 304L and 1020 are close to each other. However, it is concluded that in the current study more experimental data are needed to have an accurate assessment for the quantitative comparison of the strain rate dependency of the flow stress of the materials tested. To relate the experimental observations to high rate material data, a parametric study in an optimization framework is required. With such a study optimized values of the parameters of different flow stress models can be determined such that flow stress models represent the high strain rate behavior of the material better, and much better agreement of simulation results with experimental results can be achieved.

For the Taylor impact simulations performed at room temperature and impact speed ranges covered in this study, it is observed that among the four different flow stress models the Johnson–Cook model gives the best match to the experimental data when the final deformed profiles, final length and mushroomed end diameter are used in the comparison of experimental and simulation data.

References

1. Taylor, G.I.: The use of flat-ended projectiles for determining dynamic yield stress: I, Theoretical considerations. *Proc. R. Soc. Lond. Ser. A, Math. Phys. Sci.* **194**, 289–300 (1948)
2. Hawkyard, J.B.: A theory for the mushrooming of flat-ended projectiles impinging on a flat rigid anvil using energy considerations. *Int. J. Mech. Sci.* **11**, 313–333 (1968)
3. Jones, S.E., Gillis, P.P.: Analytical modeling of high rate processes. AFRL-MN-EG-TR-1998-7044 (1998)
4. Jones, S.E., Gillis, P.P.: Dynamic testing of materials. AFRL-MN-EG-TR-2002-7001 (2002)
5. Wilkins, M.L.: Calculation of elastic-plastic flow. UCRL-7322, Rev. I, Lawrence Radiation Laboratory, University of California (1963)
6. Johnson, G.R.: EPIC-2, a computer program for elastic-plastic impact computations in two dimensions plus spin. Technical Report ARBRL-CR-00373, Honeywell Inc. Defence Systems Division (1978)
7. Hallquist, J.O.: User's manual for DYNA2D—An explicit two-dimensional hydrodynamic finite element code with interactive rezoning. Lawrence Livermore National Laboratory, UCID-18756, Rev. 2 (1984)
8. Century Dynamics Inc.: AUTODYN theory manual. <http://www.century-dynamics.com>. Accessed 06 December 2010
9. Zukas, J.A.: Introduction to Hydrocodes. Elsevier, Oxford, UK (2004)
10. Johnson, G.R., Holmquist, T.J.: Evaluation of cylinder-impact test data for constitutive model constants. *J. Appl. Phys.* **64**, 3901–3910 (1988)
11. Holt, W.H., Mock, W. Jr., Zerilli, F.J., Clark, J.B.: Experimental and computational study of the impact deformation of titanium Taylor cylinder specimens. *Mech. Mater.* **17**, 195–201 (1994)
12. Celentano, D.J.: Thermomechanical analysis of the Taylor impact test. *J. Appl. Phys.* **91**, 3675–3686 (2002)
13. Belytschko, T., Liu, W.K., Moran, B.: *Nonlinear Finite Elements for Continua and Structures*. Wiley, Chichester, UK (2000)
14. Konokman, H.E.: Development of lagrangian hydrocode for high speed impact analysis and its experimental verification. MSc Thesis, Middle East Technical University, Turkey (2008)
15. Wilkins, M.L.: *Computer Simulation of Dynamic Phenomena*. Springer, Berlin (1999)
16. Johnson, G.R., Stryk, R.A., Holmquist, T.J., Beissel, S.R.: Numerical algorithms in a lagrangian hydrocode. WL-TR-1997-7039 (1997)
17. Johnson, G.R., Cook, W.H.: A constitutive model and data for metals subjected to large strains, high strain rates and temperatures. In: *Proceedings of 7th International Symposium on Ballistics*, The Netherlands (1983)

18. Steinberg, D.J., Lund, C.M.: A constitutive model for strain rates from 10^{-4} to 10^6 s^{-1} . *J. Appl. Phys.* **65**, 1528–1533 (1989)
19. Zerilli, F.J., Armstrong, R.W.: Dislocation-mechanics based constitutive relations for material dynamics calculation. *J. Appl. Phys.* **61**, 1816–1825 (1987)
20. Follansbee, P.S., Kocks, U.F.: A constitutive description of the deformation of copper based on the use of mechanical threshold stress as an internal state variable. *Acta Metal.* **36**, 81–93 (1988)
21. Goto, D.M., Bingert, J.F., Reed, W.R., Garrett, R.K. Jr.: Anisotropy-corrected MTS constitutive strength modeling in HY-100 steel. *Scr. Mater.* **42**, 1125–1131 (2000)
22. Varshni, Y.P.: Temperature dependence of the elastic constants. *Phys. Rev. B* **2**, 3952–3958 (1970)
23. Beissel, S.R., Johnson, G.R.: Large-deformation triangular and tetrahedral element formulations for unstructured meshes. *Comput. Methods Appl. Mech. Eng.* **187**, 469–482 (2000)
24. Detournay, C., Dzik, E.: Nodal mixed discretization for tetrahedral elements. In: *Proceedings of 4th International FLAC Symposium of Numerical Models and Geomechanics* Paper No: 07-02 (2006)
25. Bonet, J., Marriotti, H., Hassan, O.: An averaged nodal deformation gradient linear tetrahedral element for large strain explicit dynamic applications. *Commun. Numer. Methods Eng.* **17**, 551–561 (2001)
26. Lee, W.H.: Oil well perforator design using 2D Eulerian code. *Int. J. Impact Eng.* **27**, 535–559 (2002)
27. Nagtegaal, J.C., Parks, D.M., Rice, J.R.: On numerically accurate finite element solutions in the fully plastic range. *Comput. Methods Appl. Mech. Eng.* **4**, 153–177 (1974)
28. Banerjee, B.: An evaluation of plastic flow stress models for the simulation of high temperature and high strain rate deformation of metals. *arXiv:cond-mat/0512466v1* 1-43 (2005)
29. Martineau, R.L.: A viscoelastic model of expanding cylindrical shells subjected to internal explosive detonations. Ph.D Thesis, Colorado State University, USA (1998)
30. Konokman, H.E., Kayran, A., Özyörük, Y.: Lagrangian hydrocode formulation for large deformation problems and methods to prevent volumetric locking of triangular elements. In: *Proceedings of 4th Ankara International Aerospace Conference*, Ankara, Turkey, Paper No: AIAC-2007-072 (2007)
31. Levy, A.: Solid Particle Erosion and Erosion-Corrosion of Materials. ASM International, Ohio (1995)
32. Davidson, D.L., Lankford, J.: Fatigue crack tip plastic strain in high-strength aluminum alloys. *Fatigue Fract. Eng. Mat. Struct.* **3**, 289–303 (2007)
33. Teng, X., Wierzbicki, T., Hiermaier, S., Rohr, I.: Numerical prediction of fracture in the Taylor test. *Int. J. Solids Struct.* **42**, 2929–2948 (2005)
34. Frutschy, K.J., Clifton, R.J.: High-temperature pressure-shear plate impact experiments on OFHC Copper. *J. Mech. Phys. Solids* **46**, 1723–1743 (1998)
35. Lee, S., Barthelat, F., Hutchinson, J.W., Espinosa, H.D.: Dynamic failure of metallic pyramidal truss core materials—experiments and modeling. *Int. J. Plast.* **22**, 2118–2145 (2006)
36. Xue, Q., Meyers, M.A., Nesterenko, V.F.: Self organization of shear bands in stainless steel. *Mat. Sci. Eng. A* **384**, 35–46 (2004)
37. Karpp, R.R.: Warhead simulation techniques: hydrocodes. In: Carleone, J. (ed.) *Tactical Missile Warheads*, pp. 233–314. AIAA Inc., Washington, DC (1993)
38. Banerjee, B.: MPM Validation: Sphere-cylinder impact tests: Energy balance. Report No. C SAFE-CD-IR-04-001, University of Utah, Utah, USA (2004)
39. Chhabildas, L.C., Konrad, C.H., Mosher, D.A., Reinhart, W.D., Duggins, B.D., Trucano, T.G., Summers, R.M., Peery, J.S.: A methodology to validate 3D arbitrary Lagrangian Eulerian codes with applications to Alegra. *Int. J. Impact Eng.* **23**, 101–112 (1999)
40. Fish, J., Oskay, C., Fan, R.: AL 6061-T6-Elastomer impact simulations. RPI research reports <http://www.scorec.rpi.edu/cgi-bin/reports/Search3.pl?InputID=370> (2005). Accessed 06 December 2010